npj | climate and atmospheric science

www.nature.com/npjclimatsci

ARTICLE OPEN

Check for updates

Record-high Antarctic Peninsula temperatures and surface melt in February 2022: a compound event with an intense atmospheric river

Irina V. Gorodetskaya[1,2]✉, Claudio Durán-Alarcón[1,2], Sergi González-Herrero[3,4], Kyle R. Clem[5], Xun Zou[6], Penny Rowe[7], Paola Rodriguez Imazio[8], Diego Campos[9], Christophe Leroy-Dos Santos[2,10], Niels Dutrievoz[2,10], Jonathan D. Wille[11,12], Anastasiia Chyhareva[13,14], Vincent Favier[12], Juliette Blanchet[12], Benjamin Pohl[15], Raul R. Cordero[16], Sang-Jong Park[17], Steve Colwell[18], Matthew A. Lazzara[19], Jorge Carrasco[20], Adriana Maria Gulisano[21,22,23], Svitlana Krakovska[13,14], F. Martin Ralph[6], Thomas Dethinne[24,25] and Ghislain Picard[12]

The Antarctic Peninsula (AP) experienced a new extreme warm event and record-high surface melt in February 2022, rivaling the recent temperature records from 2015 and 2020, and contributing to the alarming series of extreme warm events over this region showing stronger warming compared to the rest of Antarctica. Here, the drivers and impacts of the event are analyzed in detail using a range of observational and modeling data. The northern/northwestern AP was directly impacted by an intense atmospheric river (AR) attaining category 3 on the AR scale, which brought anomalous heat and rainfall, while the AR-enhanced foehn effect further warmed its northeastern side. The event was triggered by multiple large-scale atmospheric circulation patterns linking the AR formation to tropical convection anomalies and stationary Rossby waves, with an anomalous Amundsen Sea Low and a record-breaking high-pressure system east of the AP. This multivariate and spatial compound event culminated in widespread and intense surface melt across the AP. Circulation analog analysis shows that global warming played a role in the amplification and increased probability of the event. Increasing frequency of such events can undermine the stability of the AP ice shelves, with multiple local to global impacts, including acceleration of the AP ice mass loss and changes in sensitive ecosystems.

npj Climate and Atmospheric Science (2023)6:202 ; https://doi.org/10.1038/s41612-023-00529-6

INTRODUCTION

The global average surface temperature has significantly increased during the twentieth and early twenty-first century, with temperatures 1.09 °C [0.95–1.20 °C] higher in 2011–2020 compared to the preindustrial period (1850–1900), and with each of the last four decades successively warmer than all previous decades[1]. In addition, according to the World Meteorological Organization report[2], the past 7 years have been the seven warmest on record. This global warming has been unequivocally linked to anthropogenic greenhouse gas increase and has affected every region on Earth[1]. The Antarctic Peninsula (AP) is one of the fastest warming regions in the Southern Hemisphere, exhibiting an emerging polar warming amplification[3–5]. The warming trend since the 1950s has been most pronounced in the northern and northwestern AP: at Faraday–Vernadsky station the annual mean warming trend has been 0.46 °C ± 0.15 °C per decade during 1951–2018 (in total 3.12 °C ± 1.02 °C over 68 years), and Esperanza station has warmed by 0.29 °C ± 0.16 °C per decade during 1957–2016 (in total 1.74 °C ± 0.96 °C over 60 years)[3,4] (see Fig. 1 for the stations' locations). Significant warming trends of smaller intensity have been recorded since the 1950s at Bellingshausen and O'Higgins stations north of the AP[3,4]. The short-term cooling or absence of warming recorded at some stations during 1999–2016 has not obviated this long-term trend, occurring since the 1950s[3,6–8].

Along with the global average temperature increase, most land regions have experienced a significant increase in both the frequency and intensity of warm extremes (including heatwaves) since the 1950s[9]. The AP has also been tending towards higher amplitude and longer periods of the temperature extremes during 1979–2019[10]. Warm extremes can have a significant and immediate impact on the cryosphere by inducing positive feedbacks that reinforce and accelerate the warming trend (e.g., via the ice/snow-albedo feedback). Temperature extremes have been shown to have strong impacts on surface melt on the AP ice shelves[11–13]. Turner et al.[10] examined temperature extremes at the Antarctic

[1]Interdisciplinary Centre of Marine and Environmental Research (CIIMAR), University of Porto, Terminal de Cruzeiros do Porto de Leixões, Avenida General Norton de Matos, S/N, 4450-208 Matosinhos, Portugal. [2]Centre for Environmental and Marine Studies (CESAM), Department of Physics, University of Aveiro, Aveiro, Portugal. [3]WSL Institute for Snow and Avalanche Research SLF, Davos, Switzerland. [4]State Meteorological Agency (AEMET), Antarctic Group, Barcelona, Spain. [5]Victoria University of Wellington, Wellington, New Zealand. [6]Center for Western Weather and Water Extremes (CW3E), Scripps Institution of Oceanography, University of California San Diego, San Diego, CA, USA. [7]NorthWest Research Associates, Seattle, WA, USA. [8]CONICET-Servicio Meteorológico Nacional, Buenos Aires, Argentina. [9]Dirección Meteorológica de Chile, Santiago, Chile. [10]Laboratoire des Sciences du Climat et de l'Environnement, LSCE-IPSL, CEA-CNRS-UVSQ, Université Paris-Saclay, Gif-sur-Yvette, France. [11]Institute for Atmospheric and Climate Science, ETH Zurich, Zurich, Switzerland. [12]Institut des Géosciences de l'Environnement, CNRS/UGA, Saint Martin d'Hères, France. [13]Ukrainian Hydrometeorological Institute, Kyiv, Ukraine. [14]National Antarctic Scientific Center of Ukraine, Kyiv, Ukraine. [15]Biogéosciences, CNRS/Université de Bourgogne Franche-Comté, Dijon, France. [16]Universidad de Santiago de Chile, Av. Bernardo O'Higgins, 3363 Santiago, Chile. [17]Korea Polar Research Institute, Incheon, Republic of Korea. [18]British Antarctic Survey, Cambridge, UK. [19]Madison Area Technical College and University of Wisconsin-Madison, Madison, WI, USA. [20]Centro de Investigación GAIA Antártica (CIGA), Universidad de Magallanes, Punta Arenas, Chile. [21]Instituto Antártico Argentino, Dirección Nacional del Antártico, Buenos Aires, Argentina. [22]Instituto de Astronomía y Física del Espacio, CONICET–UBA, Buenos Aires, Argentina. [23]Departamento de Física, Facultad de Ciencias Exactas y Naturales, Universidad de Buenos Aires, Buenos Aires, Argentina. [24]UR Sphère, Laboratory of Climatology, University of Liège, Liège, Belgium. [25]UR Sphère, Laboratory of Earth Observation and Ecosystem Modelling, University of Liège, Liège, Belgium. ✉email: irinag@ciimar.up.pt

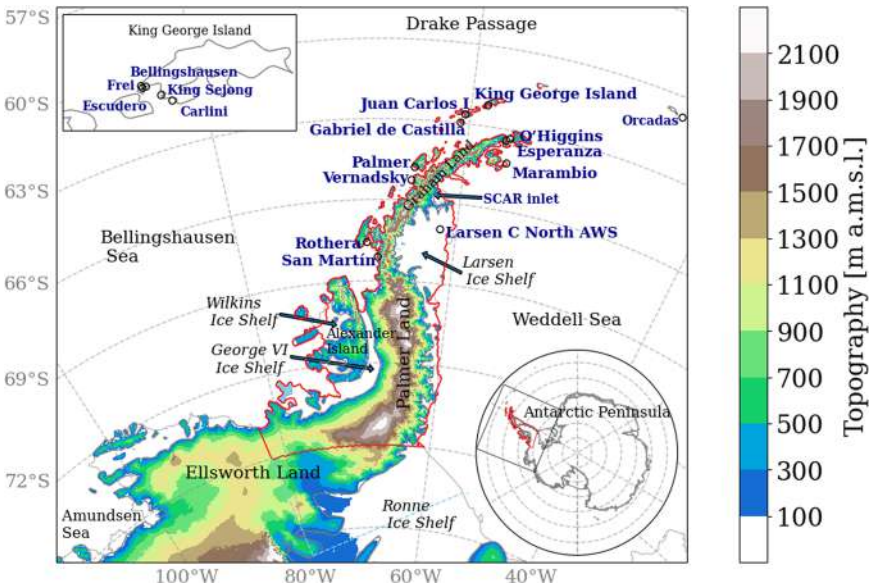

Fig. 1 Map of AP with geographic names. Location of the weather stations (black circles with bold dark blue names), ice shelves (names in black italic) and other geographical features used in this study. The topography is from the 1-km Reference Elevation Model of Antarctica (REMA) used in Polar WRF[75]. The ice shelves are delimited by the 1:10 million Antarctic Ice Shelf Edges[86]. Red line delineates the land and ice shelf extent corresponding to the Antarctic Peninsula used in the MAR analysis (Fig. 3).

stations using records through 2019, finding that Marambio and Esperanza stations (both located in the northeastern AP) had the highest temperature extremes during the last decade (17.1 °C and 17.5 °C, respectively, on 23 and 24 March 2015). A new record of 18.3 °C was measured at Esperanza station on 6 February 2020[10,14,15], and has been recently linked to anthropogenic global warming[16]. Meanwhile, stations located in the northwestern and northern AP did not show record high temperatures since the 1980s: Vernadsky measured its last record-high temperature of 10.9 °C on 25 January 1985 and 31 December 1988[10] (reaching up to 11.8 °C in January 1985 according to[17]), and Bellingshausen measured a record of 11.2 °C on 29 January 1982[11].

Warm weather episodes in Antarctica are caused by heat (and moisture) transported via transient weather systems, which form over the Southern Ocean at lower latitudes, propagate eastward and poleward and dissipate thus losing their baroclinic energy, near the Antarctic continent[18–20]. When a strong ridging or blocking high-pressure system occurs over the Southern Ocean, such cyclones can become stationary for several days, pumping moisture and heat from subtropical or mid latitudes to Antarctica[21–24] thereby forming the most favorable conditions for development of atmospheric rivers (ARs)—long corridors of high integrated moisture content and flux—landfalling in Antarctica[25–29]. ARs can also be driven by other factors such as anomalously high moisture content in the subtropics and mid latitudes, large-scale dynamics, moisture convergence, and a train of cyclones replenishing moisture [e.g., refs. [30–33]].

ARs lead to strong positive anomalies in temperature, moisture and winds along the Antarctic coast[34] and have been shown to affect all regions of the Antarctic ice sheet triggering both intense snowfall[25,26,33,35] as well as major surface melt events[36,37], related to destabilization of the AP ice shelves[38] and reappearance of polynyas[39]. The two most recent temperature records in the northeastern AP (in March 2015 and February 2020) were both linked to ARs that combined with an intensified foehn effect[15,36], triggering record warm events in the northeastern AP. Clem et al.[29] linked these ARs to enhanced central tropical Pacific convection (and El Niño-like SST anomalies), which triggered a Rossby wave train towards Antarctica. The latter deepened the Amundsen Sea Low and built a record-breaking high-pressure system over the Drake Passage[16], thereby directing the AR towards the AP. While Rossby wave packets provide teleconnection pathways between the upstream and downstream weather systems and are often precursors to high-impact extreme weather events[40,41], ARs embedded in these systems can provide a direct link between subtropical moisture and Antarctic extreme weather events[29,33].

This study details the most recent extreme warm event over the AP in February 2022 and demonstrates that it had some similarities to the previous February 2020 and March 2015 temperature extremes, but also demonstrated important differences in the planetary-scale modes of variability. The novelty of our work is that it combines multi-scale atmospheric circulation drivers, spanning from the tropics to midlatitudes, together with the moisture sources and path diagnostics, thereby enlarging our understanding of key processes (and their interconnection) that are responsible for the major AP extreme warm periods and surface melt. Our analysis is based on a range of observational and modeling data, including near-surface observations of temperature, radiosonde observations of the troposphere and lower stratosphere structure, snow melt occurrence from satellite microwave observations, ERA5 reanalysis for large-scale atmospheric circulation and AR analysis, 7.5-km spatial resolution simulations over the AP domain with the regional climate model MAR (Modèle Atmosphérique Régional) with advanced multilayer snow model for snow melt amount estimates, 1.2-km spatial resolution dynamical downscaling over the AP using non-hydrostatic Weather Research and Forecasting model adapted for the Polar regions (Polar WRF) for local drivers analysis, and FLEXPART Lagrangian particle dispersion model with ERA5 input for moisture sources and pathways analysis (see Methods). Here we build on the knowledge gained from previous studies of AR-related heatwaves over the AP[16,29,36], presenting an even more extensive view of the driving mechanisms adding other key "ingredients" responsible for the AR "flavors" and the intensity of their impacts on the AP. Given the increasing frequency of occurrence of extreme heat events, it is important to understand the processes and mechanisms leading to their development, and make sure that both operational forecast and climate models can represent them correctly.

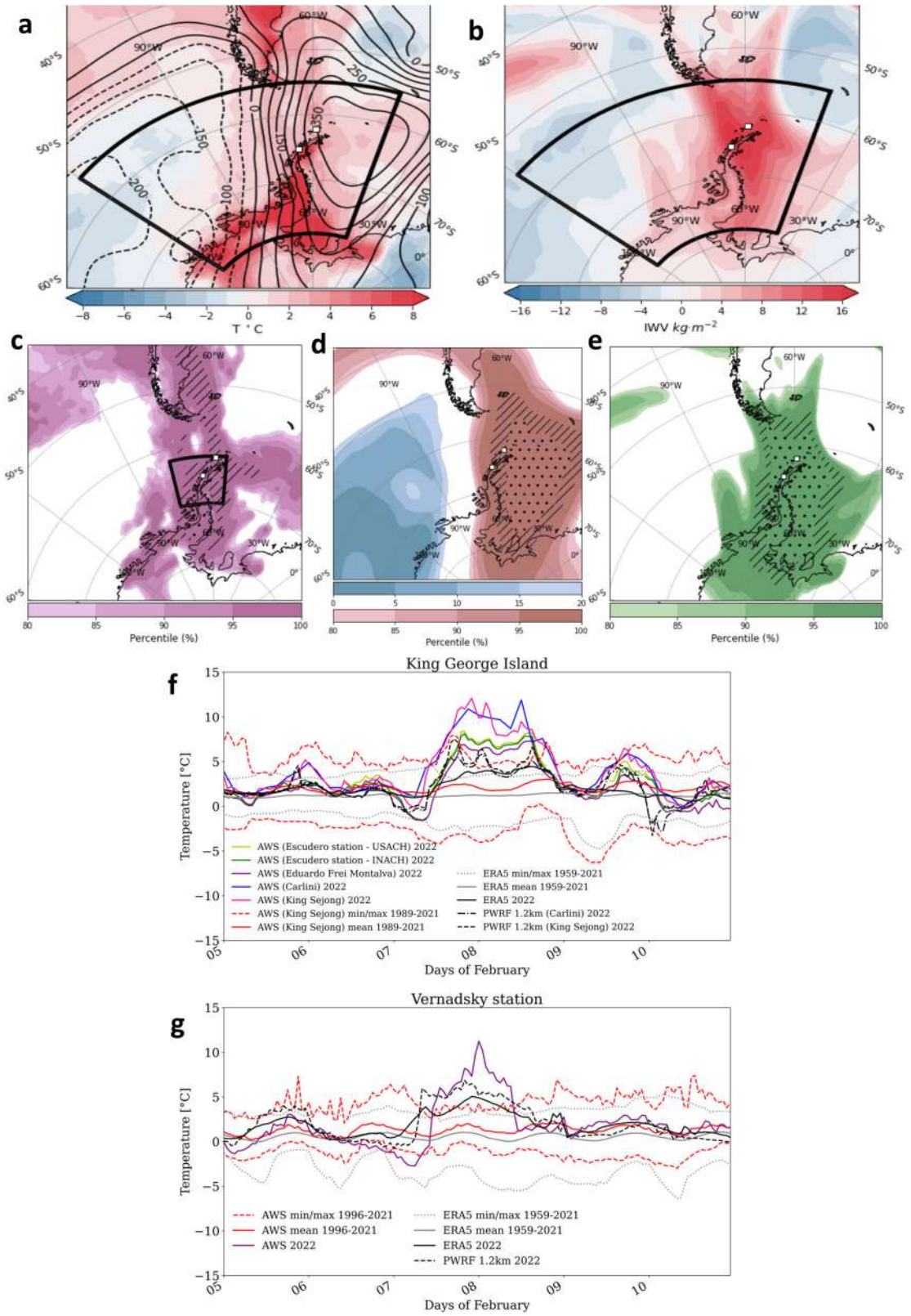

RESULTS

AP temperature and surface melt records

On 7-8 February 2022, extreme high near-surface temperatures were recorded at several stations around the AP, with record high values measured at two stations located on King George Island (13.7 °C at King Sejong and 13.6 °C at Carlini) and at two stations in the northwestern AP (11.6 °C at Palmer and 12.7 °C at Vernadsky) (see Fig. 1 for the AP locations and topography, Fig. 2, Supplementary Fig. 1, and Supplementary Table 1). These temperatures broke the previous records since continuous

Fig. 2 Temperature, pressure and moisture extremes during the February 2022 hot spell. Anomalies of **a** near-surface temperature (°C, shaded) and 500-hPa geopotential height (gpm, contours) and **b** integrated water vapor (IWV, kg m^{-2}) for 7 and 8 February 2022 wrt. summer 1959–2021 over the AP. Thick black line in (**a**, **b**) outlines the [55°–78°S; 120–40°W] region used to calculate the analogs based on the 500-hPa geopotential heights (shown in Fig. 10). **c**–**e** Percentiles of the 7 and 8 February 2022 anomalies wrt the climatological distribution of 2-day running means (based on 6-hourly values) from summer 1959–2021 for **c** temperature, **d** 500-hPa geopotential height, and **e** IWV. Hatched areas indicate values higher than the 99th percentile, and dots indicate the absolute record values. Thick black line in (**c**) outlines the [62–70°S 76–55°W] region used to calculate the analog-like temperature anomalies (shown in Fig. 10). White squares indicate the locations of King George Island and Vernadsky. **f**, **g** Time series of hourly 2-m air temperature during 1–10 February 2022 for **f** stations located on King George Island (AWS measurements at Escudero, Frei, Carlini and King Sejong, colored lines) and **g** Vernadsky station (AWS measurements, purple line) compared to the ERA5 nearest grid-average during the event (bold black), Polar-WRF 1.2-km domain output nearest grid to Carlini (black dash-dot) and King Sejong (black dash), ERA5 climatology (thin black, mean 1959–2021), observed climatology at King Sejong (red, mean 1981–2021) and range based on ERA5 (black dotted line, min/max 1959–2021) and observations at King Sejong (red dotted line, min/max 1989–2021).

measurements began at each station, in 1988 at King Sejong, 1985 at Carlini, 1989 at Palmer and 1948 at Faraday–Vernadsky. Extremely high hourly temperatures at King Sejong were observed for slightly more than 2 days and the warmest period (hourly values above 6.1 °C, which is the 99th percentile for all months of February, 1988–2022) lasted 32 h (from 9 UTC on 7 February until 16 UTC on 8 February) (Fig. 2f and Supplementary Fig. 1a, c). The peak temperatures observed at Carlini station followed those at King Sejong with the highest temperature peak reached in the beginning of this period (Fig. 2f). Vernadsky station had a shorter anomalously warm period with the record-breaking peak of 12.7 °C (1-min temperature measurements) registered by automatic weather station (AWS) measurements at 23 UTC on 7 February 2022, while the extreme warm period (hourly values above 5.1 °C, which is the 99th percentile for all months of February, 1996–2018) lasted 23 h (from 11 UTC on 7 February until 09 UTC on 8 February) (Fig. 2g and Supplementary Fig. 1b, d). Other AP stations recorded extremely high temperatures (all exceeding 98th percentile and for some 99th or 99.9th percentiles for each station measurement time period), although they did not break the absolute records established for these stations (Supplementary Table 1).

The event had a significant spatial extent and intensity according to ERA5 reanalysis data: two-day mean temperatures (during 7 and 8 February) across most of the AP were anomalously high by more than 5 °C (Fig. 2a) and above the 99th percentile of all summer two-day mean temperatures from 1959 to 2021 (Fig. 2c). Moreover, an extensive part of the Bellingshausen and Weddell Seas had two-day temperature anomalies above the 95th percentile (Fig. 2c) and the two-day geopotential height records were broken over most of the Weddell Sea (Fig. 2d). Record-breaking values of the two-day mean integrated water vapor (IWV) spanned Bellingshausen Sea, the AP and a large part of the Weddell Sea (Fig. 2b, e). The high magnitude and large extent of the temperature anomalies along with the large affected area but a relatively short duration (two days) allows this event to be classified as a hot spell rather than a heatwave, which is usually characterized by a longer persistence of at least 3 days (e.g., ref. [42]). For comparison, the 6-day heatwave over the AP during February 2020 affected a smaller Antarctic region and a larger mid-latitude oceanic region[16]. A particular feature of the February 2022 event is the occurrence of maximum daily temperatures over the AP during the local evening/night hours (between 7 February, 21 UTC and 8 February, 00 UTC) when surface net shortwave (SW) radiation was approaching zero (the role of radiative and turbulent fluxes in temperature increase is presented in section "Atmospheric river and local drivers").

During this hot spell event, the AP received a significant amount of snowfall over Palmer and Ellsworth Lands, while all its coastal regions and the ice shelves were mainly affected by rainfall (Fig. 3a, b based on a 7.5-km spatial resolution simulation with the regional climate model MAR over the AP, see "Methods"). Rainfall was particularly intense, with daily total rainfall averaged over the AP up to 18 mm water equivalent (w.e.), the largest daily value during February since 1980 (according to MAR model, Fig. 3g). In the northwestern AP, where rainfall was more intense, orographic precipitation enhancement played a significant role, producing large contrast between upstream and downstream areas. The topographic effect was well reproduced by the high-resolution (1.2-km) Polar WRF model (Supplementary Fig. 2a and Figs. 7 and 8 in Zou et al.[43]). At the Vernadsky station, located on the Galindez Island in the northwestern AP coast, the rainfall rate was slightly above 10 mm per day (derived from the MRR-PRO radar measurements, and also ERA5 reanalysis and Polar WRF model; see Methods), while the rainfall rate in the nearby slopes of the Kyiv Peninsula was more than 80 mm w.e. per day (according to the Polar WRF model, Supplementary Fig. 2a). The MAR model, despite its coarser resolution, also showed an increase in rainfall due to the topography in northwestern AP, although with lower values compared to the Polar WRF 1.2-km runs (Fig. 3b and Supplementary Fig. 2b). These contrasting rainfall values illustrate the large precipitation variability occurring at small spatial scales and the difficulties to model precipitation in complex terrain in Antarctica.

Moreover, the hot spell caused widespread surface melt on both the western and eastern sides of the AP with daily accumulated magnitude reaching 6.2 Gt on 8 February averaged over the AP (north of 75°S latitude, see the exact area in Supplementary Table 2 and Fig. 3d for the maximum surface melt extent). Both the area covered by melt and the total daily amount reached record-high values over the period 1980–2022 based on the MAR model estimates (Fig. 3e, f). Surface melt affected the remaining intact AP ice shelves over their entire area (according to satellite observations, Fig. 3d) with the daily values exceeding 80 mm w.e. accumulated over the 4 days from 6 to 9 February over the Larsen C, George VI and Wilkins ice shelves (Fig. 3c, estimate based on MAR). These remaining ice shelves have been deemed vulnerable to hydrofracturing-caused destabilization (due to excessive surface melt water) in a warming climate[12,13,44,45]. The snow status (wet or dry) derived from satellite observations confirms the large extent of melt occurrence over the AP ice shelves (Fig. 3d), with MAR showing a good agreement, while ERA5-Land strongly underestimates the melt area. During February 2022, the area of the AP and its ice shelves affected by snowmelt reached a new record high (of 257,741 km^2 or 52% of the total AP area) according to satellite observations since 2003 for this period of the year, while MAR showed a larger snowmelt extent covering 73% of the AP (Fig. 3d, e and Supplementary Table 2). This slightly exceeded the February 2020 previous record (by 2% according to satellite observations and by 11% according to the MAR model) (Fig. 3e, Supplementary Table 2, and Supplementary Fig. 3b–e). Furthermore, satellite observations indicate that the entire Larsen C ice shelf area was affected by melt, with MAR pointing to the northern part as having one of the highest melt amounts (Fig. 3c).

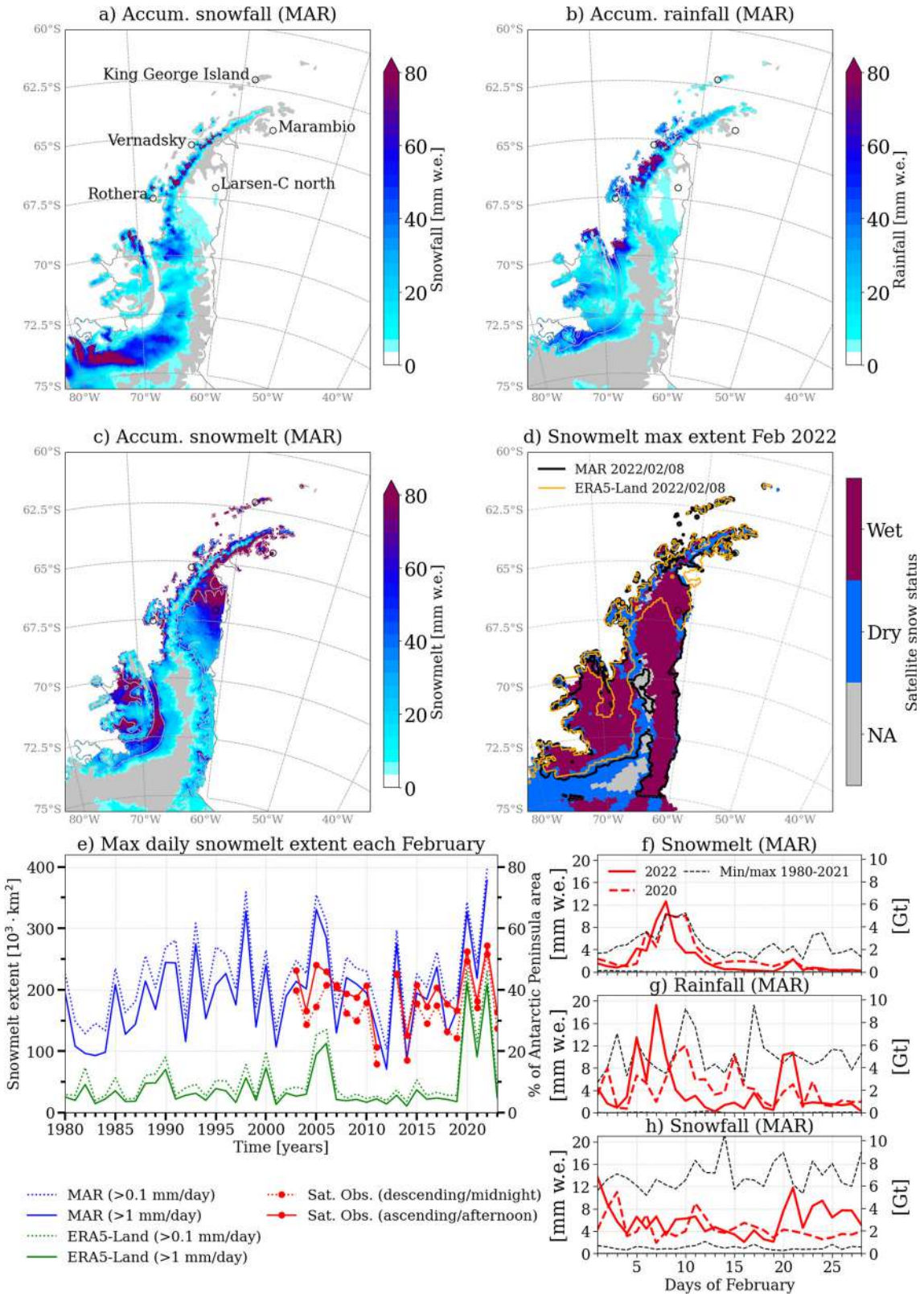

Atmospheric river and local drivers

These temperature and snow melt anomalies were brought by an AR that first made landfall in southern South America, and then the AP (Fig. 4), where it combined with a foehn effect on the lee side in the vicinity of the AP mountain range (Fig. 5, see ref. [43] for detailed foehn analysis). Heat and moisture advection from the Pacific directly affected the northern and northwestern AP in the upstream side of the AP topographic barrier, maintaining near-surface temperatures above 0 °C over the region even during the night, when they reached their peak during the event (Fig. 2d, e).

Fig. 3 Surface snowmelt and precipitation over AP during the February 2022 hot spell. Accumulated **a** snowfall, **b** rainfall, and **c** surface snowmelt during the duration of the event 6–9 February 2022 (all based on MAR). **d** Snowmelt maximum extent during the 6–9 February 2022 period defined as wet/dry/not-assigned (NA) snow status derived from microwave satellite observations brightness temperatures[77] compared with the maximum melt extent from MAR (black line) and ERA5 (orange line). **e** Time series of maximum daily extent of snowmelt during February derived from satellite observations (red), MAR (blue) and ERA5-Land (green). MAR and ERA5-Land show the maximum melt extent using two different thresholds, >0.1 mm w.e. day^{-1} (dotted line) and >1 mm w.e. day^{-1} (solid line), while satellite observations (AMSR-E and AMSR-2), show the ascending (local afternoon) and descending (local midnight) overpasses (solid and dashed lines, respectively). **f** Daily accumulated snowmelt (left axis: mm w.e., right axis: Gt) averaged over the AP during February 2022 (red solid line) compared to the February 2020 values (red dashed), as well as the total range (min to max) (black dotted) during 1980–2021 (based on MAR). **g**, **h** same as (**f**) but for rainfall and snowfall, respectively (based on MAR). The ice shelf edges are based on ref. [86].

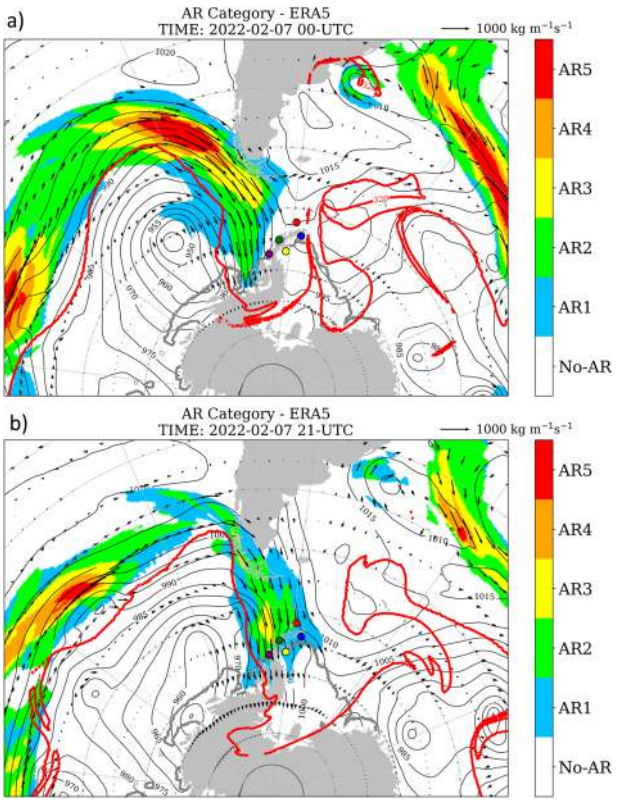

Fig. 4 Atmospheric river and Rossby wave breaking. AR scale (shading), integrated vapor transport (IVT) vectors (kg m^{-1} s^{-1}, black arrows), mean sea level pressure (hPa, black contours), 320-K potential temperature on the dynamic tropopause (−2 PVU surface) (thick red line) and sea ice edge (identified as the 10% sea ice concentration) (thick gray line) for 7 February 2022 at **a** 00 UTC and **b** 21 UTC. Colored circles show station locations: King George Island (red), Vernadsky (green), Rothera (brown), Marambio (blue), and Larsen C north AWS (yellow). Based on ERA5 reanalysis.

The category-5 AR (an extreme intensity according to the classification of Ralph et al.[46]) with IVT above 1000 kg m^{-1} s^{-1} reached the western coast of Chile, causing severe winds and rainfall on 7 February 2022 at around 06 UTC (Fig. 4a). Southern South America was also affected by the warm anomalies (Fig. 2a, c), which makes it a spatially compounding event (according to the definition by Zscheischler et al.[47], when the impact is spatially aggregated with the extreme phenomenon affecting multiple distant locations). While still affecting southern South America, the AR rapidly progressed southward, reaching the AP's northern and northwestern parts on 7 February: an intense and almost strictly meridional moisture flux traversed the Drake Passage and the entire Bellingshausen Sea along the AP western coast, landfalling in Ellsworth Land (Fig. 4a and Supplementary Fig. 4). The AR reached its peak intensity over the AP on 7 February, 21 UTC, attaining category 3 on the AR scale, which is a rarely observed high AR intensity for this cold region (with IVT values up to 600–650 kg m^{-1} s^{-1} at the western and northern AP) (Fig. 4b and Supplementary Fig. 4). The event continued until February 9, around 12 UTC, with exceptionally high IWV concentrated over the Weddell Sea (more than 10 mm and 10–12 standard deviations above average, Supplementary Fig. 5) and a corridor of high IVT now stretching from the Atlantic Ocean (Supplementary Fig. 4). The absolute daily-mean IWV showed extremely high values over the Drake Passage, Bellingshausen Sea and Weddell Sea during 7 and 8 February (Fig. 2b, e and Supplementary Fig. 5a, b), persisting over the Weddell Sea during 8 and 9 February with daily-mean values above 22 mm (Supplementary Fig. 5b, d), which were the days with the highest IWV values ever recorded in the Weddell Sea since 1979 based on ERA5 (Supplementary Fig. 5d). Thus, in addition to spatially compounding, it is also as a multivariate compound event as several variable extremes affect the same region simultaneously[47].

While near-surface temperatures were anomalously high, the maximum temperature, absolute humidity and wind speed on the upstream side of the AP barrier occurred above the surface at the 900–925 hPa level, within the layer containing the maximum AR moisture flux (according to radiosonde observations from King George Island, Fig. 6d and Supplementary Fig. 6). On 8 February at 00 UTC near-surface temperature was 7.5 °C and specific humidity was 4 g kg^{-1}, while much higher values (13 °C and 8 g kg^{-1}, respectively) were observed at 920–930 hPa (620–700 m above sea level (ASL)) for temperature and at 950 hPa (450 m ASL) for humidity (Fig. 6a, b). Wind speed increased from 8 m s^{-1} near the surface to a maximum of 25 m s^{-1} at 935 hPa level (at the height just below the temperature maximum) (Fig. 6c). The anomalously warm and moist layer extended up to 700 hPa with temperatures above 0 °C and specific humidity above 5 g kg^{-1} (Fig. 6a, b) with a strong zonal and meridional moisture flux on 7 February, 12 UTC (Fig. 6e) and exceptionally strong meridional moisture flux on 8 February, 00 UTC (up to 150 W m^{-2} at 930 hPa, Fig. 6f). Satellite measurements confirm that the AR was also characterized by meridional transport of high levels of water vapor content as well as cloud mass from the mid-latitudes into the AP region (Supplementary Fig. 7a, b) bringing a high amount of low cloud cover containing liquid water in the northern and western AP (Supplementary Fig. 7g, h).

The distribution of cloudiness and precipitation was very uneven around the AP because of its complex topography and high mountain range (Fig. 1). The northerly flow impinging on the northern AP lead to intense precipitation on the upwind side of the AP (Fig. 3a, b, based on the regional climate model MAR) and created a foehn effect enhancing high temperature anomalies on the lee side (Fig. 5a, b, based on the 1.2-km resolution Polar WRF model simulation, see Methods). The foehn-related processes are presented in detail by Zou et al.[43] using observations and Polar WRF simulations, showing that sensible heat transfer from the upper foehn flow to the surface via turbulence was the dominant contributor to surface warming during nighttime, while enhanced downwelling SW radiation (due to foehn-related cloud clearance) was the dominant contributor to surface warming on the leeside

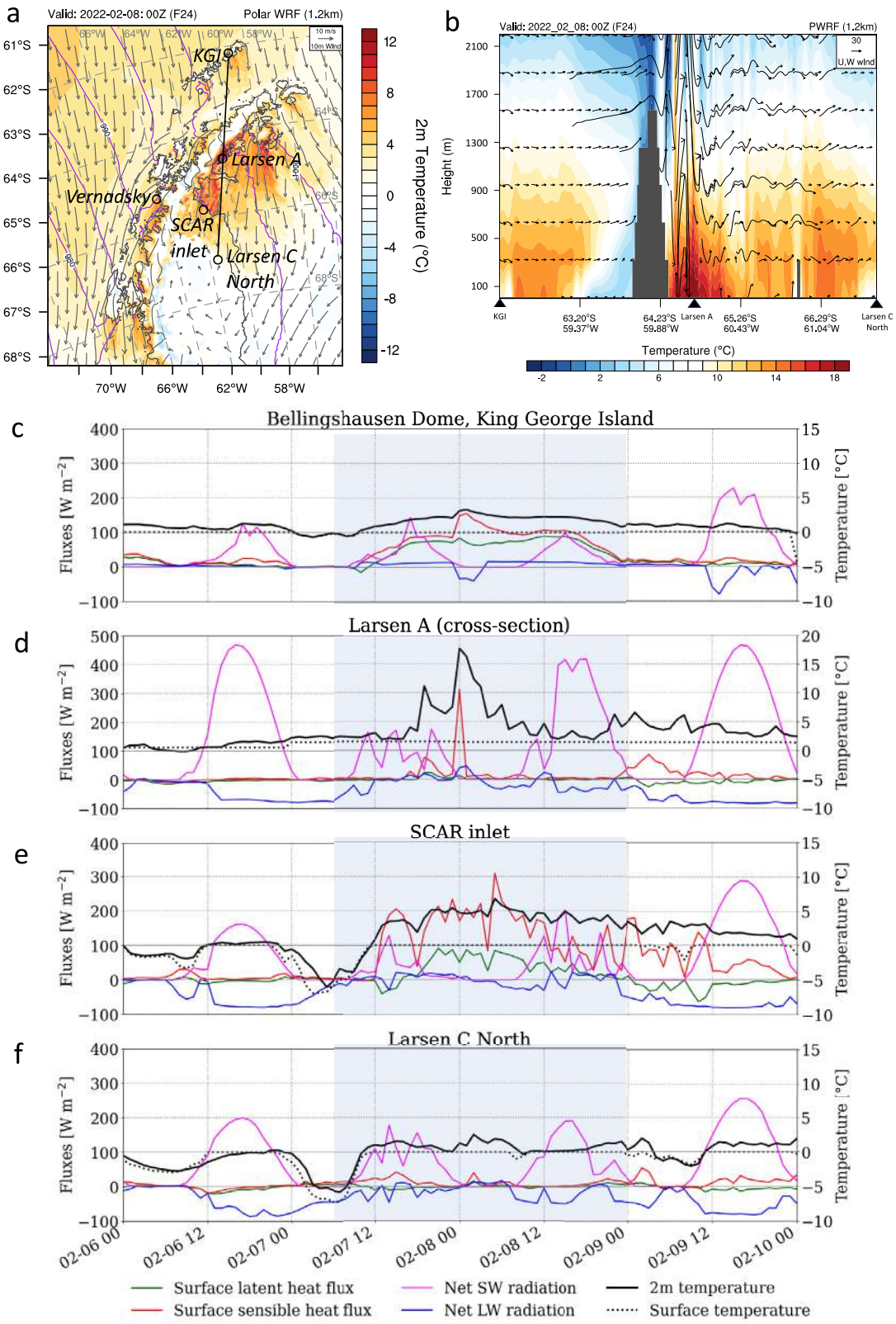

Fig. 5 **High-resolution analysis of temperature, wind and heat fluxes over the northern AP. a** 2-m air temperatures (°C, shaded), 10-m wind (m s^{-1}, vectors) and mean sea level pressure (hPa, violet contours). Thin black line indicates the cross-section in (**b**). **b** Air temperature (°C, shading) and wind (m s^{-1}, vectors, with 10× scaling for the vertical component) cross-section from King George Island (KGI, Bellingshausen Dome) to Larsen C north AWS location (passing through Larsen A) from near the surface (4-m above ground) up to 2200 m height, including topography (dark gray). **c**–**f** Time series of surface latent (green) and sensible heat fluxes (red), net SW (magenta) and net LW (blue) radiative fluxes, 2-m air temperature (black line) and skin temperature (black dots) at the point locations with ice and/or snow surfaces for **c** Bellingshausen Dome (King George Island, Collins glacier), **d** Larsen A (cross-section point), **e** SCAR inlet, and **f** Larsen C north (AWS location). All fields are the output from the Polar WRF, 1.2-km resolution domain (3-domain run forced with ERA5, see "Methods").

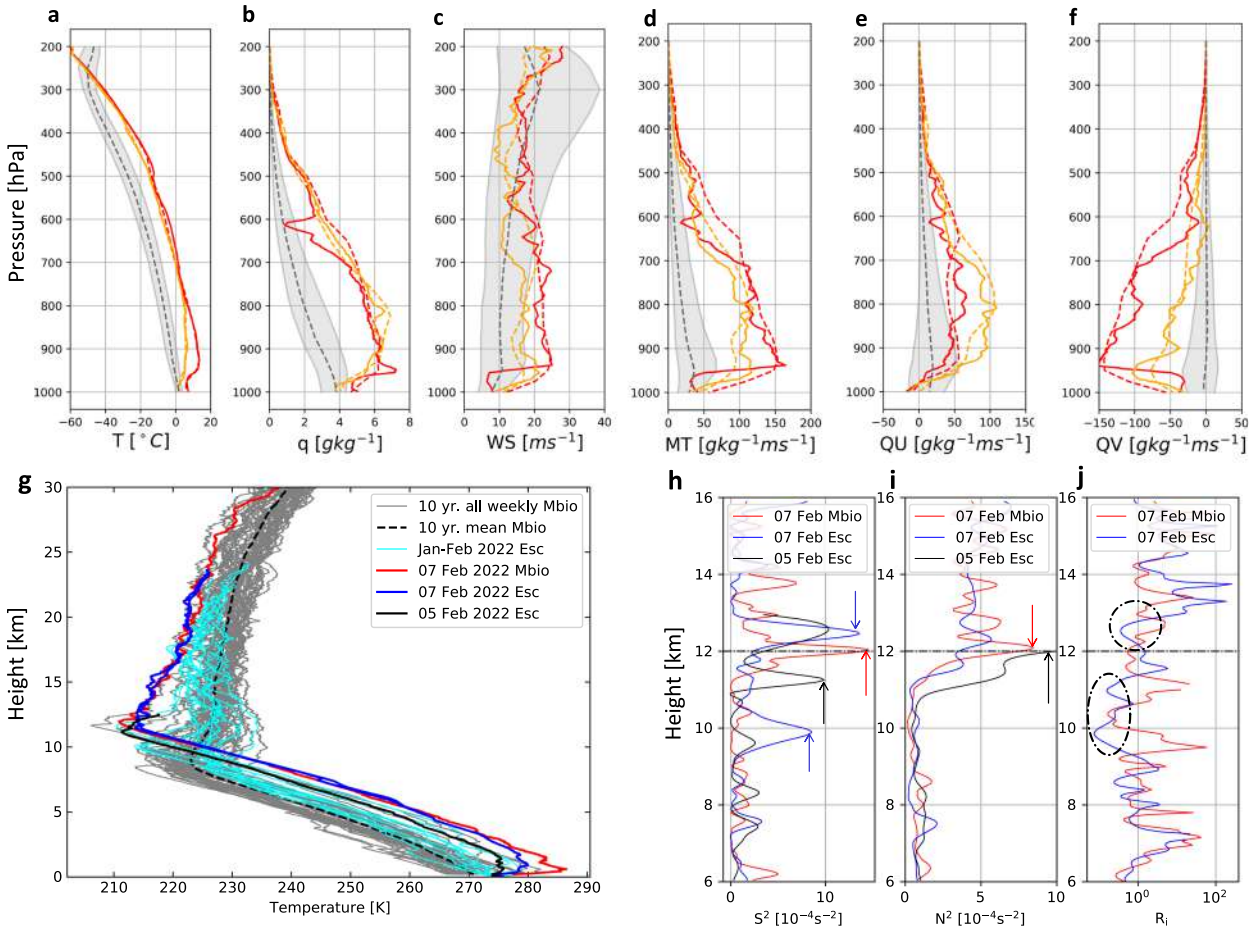

Fig. 6 Troposphere-lower stratosphere profiles at King George Island during the 7-8 February 2022 event compared to climatology. Vertical profiles of **a** temperature (T, °C), **b** specific humidity (q, g kg^{-1}), **c** wind speed (WS, m s^{-1}), **d** total moisture transport (MT, g kg^{-1} m s^{-1}), **e** zonal (QU), and **f** meridional (QV) moisture transport components from surface to 200 hPa. Based on the radiosonde measurements at the Escudero station on 7 February 12 UTC (yellow solid lines) and 8 February 00 UTC (red solid lines) and ERA5 at the nearest grid for the same times as the radiosondes (dashed yellow and red lines, respectively). The extreme event values are compared to the climatological median (black dash line) and standard deviation (gray shading) based on ERA5, January-February 1980–2022. **g** Radiosonde-measured vertical profiles of temperature on 7 February 2022, 12 UTC, at Marambio (Mbio, red), and on 5 and 7 February 2022, 12 UTC, at Escudero (Esc, black and blue, respectively) compared to 10-year mean (dash black) and all individual weekly radiosonde profiles (gray lines) at Marambio and January-February 2022 regular summer profiles at Escudero (cyan), showing how exceptional the 7 February 2022 profiles were at both stations throughout the troposphere and in the lower stratosphere (from surface to 30 km height). **h**–**j** Vertical profiles from 6 to 16 km of **h** the squared vertical wind shear (S^2), **i** the squared Brunt–Väisälä frequency (N^2), and **j** the Richardson number (Ri) estimated from radiosonde measurements. The arrows and circles indicate thresholds mentioned in the text.

during daytime (with the exception of several regions affected by mountain gap flows of moist and cloudy air). Here we highlight the role of the local radiative and turbulent heat fluxes at four different sites with ice/snow surface (along the cross-section from the northern upwind side of the AP to the leeside over the Larsen C ice shelf) that experienced melt during the 7-8 February 2022 event (Fig. 5c–f). AR heat and moisture advection brought high sensible and latent heat fluxes over the Bellingshausen Dome (Collins glacier, King George Island) and cloudy conditions (with 0 W m^{-2} surface net longwave (LW)) during the warm period (Fig. 5c). Measurements at the nearby station Escudero showed high downwelling LW radiative flux (up to 350 W m^{-2}) during the time of the near-surface temperature peak on 7 February (Supplementary Fig. 7o). The highest temperature along the cross-section occurred on the leeside at the Larsen A embayment site with a peak up to 18 °C during the nighttime at 00 UTC on 8 February associated with very high sensible heat flux (up to 300 W m^{-2}) due to the strong downslope winds (according to the Polar WRF, Fig. 5a, b, d). Enhanced near-surface air temperatures and surface melting at the SCAR inlet (the remnant of the Larsen B ice shelf, which disintegrated in 2002) were largely driven by continuous enhanced sensible heat flux (peaking at 300 W m^{-2}) and latent heat flux (up to 100 W m^{-2}) during the nighttime (Fig. 5e). The Larsen A and SCAR inlet sites are located in the leeside region affected by foehn winds with a strong downslope wind and strong temperature enhancement found in the mountain vicinity (Fig. 5b, see ref. [43] for detailed foehn processes analysis). The Larsen C north station site located further away from the AP was already beyond the foehn downslope wind zone and the peak temperatures occurred during cloudy conditions (net LW ~ 0 W m^{-2}) and negligible turbulent fluxes (Fig. 5f). Cloud clearance and increase in surface net SW radiative fluxes affect the Larsen A, SCAR inlet and Larsen C North sites during 8 February daytime and maintaining the near-surface air temperatures above 0 °C (Fig. 5d–f and Supplementary Fig. 7k–n). Thus, the high-resolution Polar WRF model simulation shows the importance of cloud LW induced warming of the surface particularly at the upwind AP side, strong sensible and latent heat flux at all locations except for northern Larsen C, and the important role of increased net SW due to cloud clearance on the leeside.

Large-scale drivers, upper troposphere configuration and moisture sources

While ARs are classified as meso- to synoptic scale features, we seek to better understand how these events are embedded in planetary-scale circulation patterns influencing their origins and evolution. The AR that reached the AP on 7 February 2022 was associated with a large and anomalously deep extra-tropical cyclone first centered over the Amundsen Sea on 4 February, then deepening and expanding northward with a secondary center developing north of the Amundsen Sea (Supplementary Fig. 8a, c, e). The cyclone reached its peak size (stretching from the Amundsen Sea to 35°S) and intensity on 6 February with MSLP more than 40 hPa and 4 standard deviations below normal (Supplementary Fig. 8e) and 500-hPa geopotential in the 1st–5th percentile relative to summer 1959–2021 (Fig. 2c). The cyclone then shifted eastward into the Bellingshausen Sea while gaining a positive tilt on 7 February when the AP hot spell began (Fig. 7h). A strong surface high-pressure system persisted over the Drake Passage during 4–6 February and then built poleward into the Weddell Sea on 7 and 8 February (Figs. 4 and 7 and Supplementary Fig. 8). This ridge exhibited record-breaking 500-hPa geopotential height values (Fig. 2d). Together, the deep Amundsen Sea Low - Drake Passage High couplet directed anomalous moisture originating from the sub-tropical Pacific Ocean southward to the South American coast, and then towards the AP forming an intense AR (Fig. 4 and Supplementary Fig. 4).

The AR was linked to a large-scale Rossby wave breaking (RWB) lasting from 5 to 9 of February: it is visible as a reversal of the potential temperature meridional gradient and bending of the 320-K isentrope on the dynamic tropopause (red contour in Fig. 4 and Supplementary Fig. 4). The development of the anomalously deep Amundsen Low is coupled to a pronounced cyclonic RWB (Fig. 4a), while the strengthening and semi-stationary position of the high-pressure ridge over the southern Atlantic is linked to an anticyclonic RWB (Fig. 4b). The intense AR, which caused the AP hot spell, was positioned within a narrow corridor of high potential temperatures intruding from the subtopics poleward over the AP and then Weddell Sea (Supplementary Fig. 4). The Hovmöller diagram of the meridional wind component at 500 hPa (Fig. 8) shows a Rossby wave packet over the southern Pacific Ocean moving downstream during 1–5 February, then stalling with strongly intensified southward (negative) meridional wind anomalies over the South American coast, Drake passage and northern AP during the hot spell (6–9 February), while a semi-stationary positive meridional wind anomaly persisted over the Weddell Sea from 6 February 00 UTC until 12 February.

In the following, we show that these Rossby wave anomalies and the strengthening of the Drake Passage and Weddell Sea high-pressure ridge were likely triggered by tropical convection anomalies. An extensive band of anomalous deep convection developed in the southwest and central tropical Pacific on 2 February stretching from northeast Australia to ~160°E (not shown), which persisted through 4–7 February (Fig. 7a, c, e, g). The persistent convective activity in this region occurred over the anomalous warm SSTs in the western Pacific Warm Pool and in the southwestern sub-tropical Pacific along the South Pacific Convergence Zone (SPCZ, Supplementary Fig. 9) associated with the ongoing La Niña conditions[48]. The enhanced tropical convection was preceded by a mid-latitude wave intrusion from the Tasman Sea/New Zealand region on 2 and 3 February (not shown), a common occurrence that is known to trigger deep convection in the central/southeast portion of the SPCZ[30,49]. The Madden–Julien Oscillation was limited to the Indian Ocean (a typical situation during La Niña when convection anomalies do not reach far eastward into the Pacific[50]), and although its intensity was weak, it nevertheless contributed to maintaining and concentrating deep convection there (Supplementary Fig. 10).

The deep convection in the southwest and central tropical Pacific generated strong 200-hPa divergent wind anomalies and a positive (anticyclonic vorticity forcing) Rossby wave source (RWS) developed along its southern and eastern edge during 4–7 February (Fig. 7a, c, e, g). During 4–6 February, anomalous southeast-ward directed stationary wave fluxes emanating from the anticyclonic RWS aided in building a ridge east of New Zealand (Fig. 7b, d, f) Downstream of the ridge, a negative (cyclonic vorticity forcing) RWS developed north of the Amundsen Sea during 5-6 February, accompanied by anomalous stationary wave fluxes, which coincided with the development and deepening of the secondary low to the north of the Amundsen Sea (Fig. 7c–f). Simultaneously, a positive RWS (along with anomalous stationary wave fluxes) developed east of the cyclone over the Bellingshausen Sea during 5–7 February, which appears to maintain the ridge over Drake Passage and southern South America, but especially build the ridge poleward into the Weddell Sea on 7 February (Fig. 7c–h). The anomalous stationary wave flux patterns over the 4–7 February period show a great circle Rossby wave path stretching from the central tropical Pacific convection into the mid-latitude South Pacific and South Atlantic. Based on the Rossby wave flux path and the local Rossby wave sources/vorticity forcing along the wave path, the large-scale Rossby wave was likely key to developing the secondary low-pressure center north of the Amundsen Sea (hence contributing to its elongated and double-barrel structure, i.e. with two low centers visible for 5 February, Fig. 7d and Supplementary Fig. 8c) and maintaining and building the high-pressure ridge over Drake Passage and the Weddell Sea.

Additional regions of weaker negative OLR anomalies were also present throughout the event in the subtropical and mid-latitude southern and eastern Pacific, suggestive of increased cloud cover in the extratropics, (Fig. 7a, c, e, g). They were associated with positive anomalies in the ocean surface evaporation feeding moisture to the AR reaching the AP (Fig. 9a). The surface evaporation anomalies in subtropics occurred over the region of positive sea surface temperature anomalies (Supplementary Fig. 11a). Figure 9b shows the back-trajectories, which brought anomalous moisture amounts to Vernadsky (both near the surface and at the 2-km height where precipitation formed) at the time of the temperature peak on 7 February, 21 UTC. The air parcels that reached Vernadsky on 7 February at the 50-m height were near the boundary layer gaining moisture (increasing specific humidity) from this subtropical region during 1–3 February (Fig. 9c), while the air parcels that reached Vernadsky on 7 February at 2-km height were near the boundary layer in the same subtropical region during 4 and 5 February (Fig. 9b). After that the air mass rapidly approached South America on February 6 and then the AP on February 7 losing moisture via precipitation (decreasing specific humidity, Fig. 9b, c).

According to earlier studies[51,52], compounding large-scale modes of variability can play a key role in influencing ARs reaching the AP and West Antarctica. Particularly, Clem et al.[51] showed that ENSO, SAM and the Amundsen Sea Low can have a combined effect on the AP temperatures. While the SAM was continuously positive during August 2021–May 2022 (with a value of 1.92 in February according to the index of Marshall[53]), the daily geopotential height and MSLP anomalies seen during 4–7 February (Fig. 7 and Supplementary Fig. 8) were strongly asymmetric and the pressure anomalies over Antarctica were weak and not spatially uniform. Thus, it appears the large-scale positive SAM pattern temporarily dissipated during this event.

Finally, the observed atmospheric temperatures and wind speeds in the northern AP indicate that the AR was associated with extreme conditions throughout the troposphere and the upper troposphere-lower stratosphere (UTLS) before and during the hot spell at upstream sites in the northern AP (Fig. 6g–j). Measurements by radiosondes launched from Marambio on 7

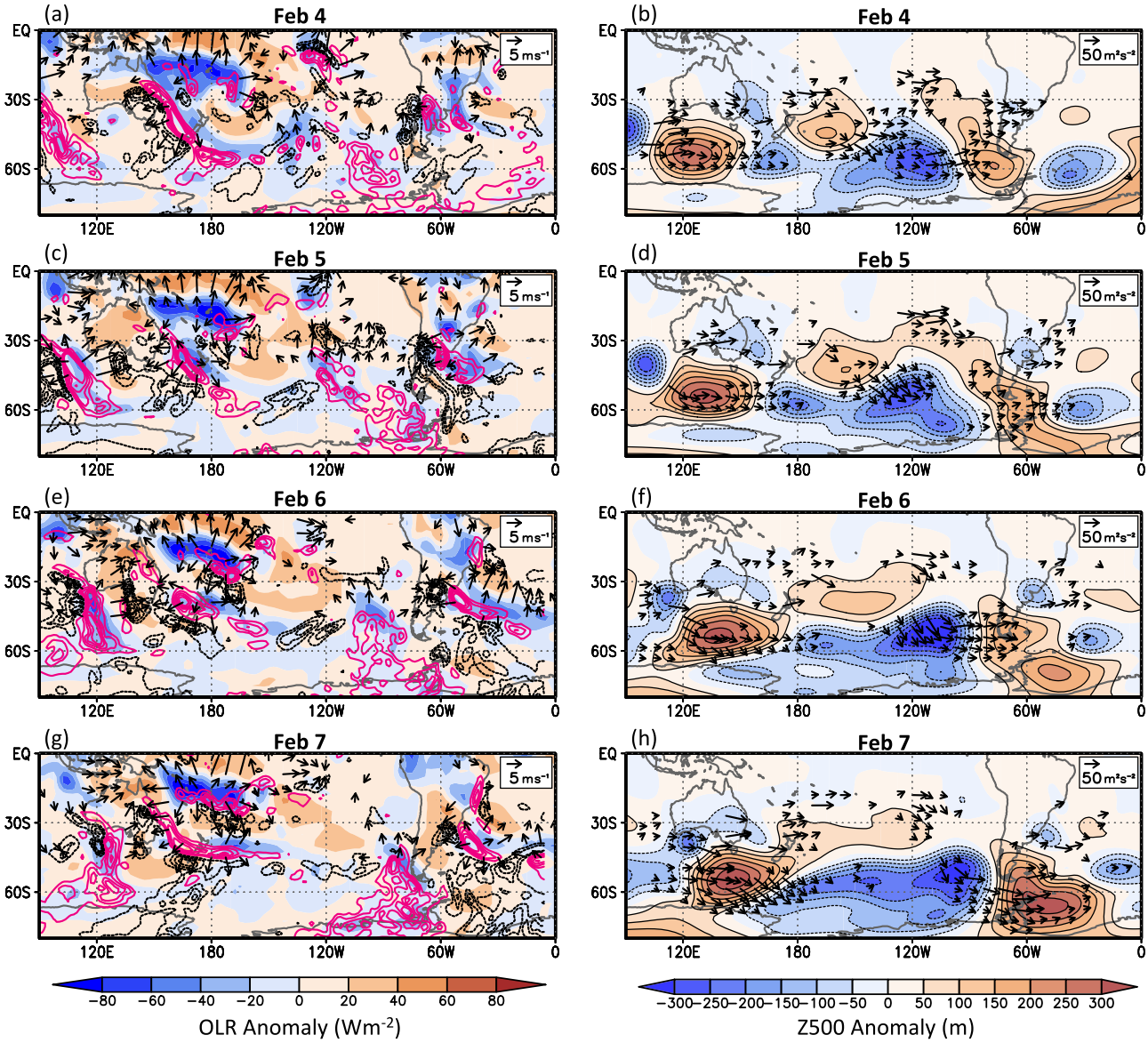

Fig. 7 Tropical convection, Rossby wave propagation and Amundsen Sea Low - Weddell Sea High couplet development. a Daily anomalies in outgoing longwave radiation (OLR; shaded) and 200-hPa divergent wind (vectors, m s^{-1}, with divergent wind speeds <3 ms^{-1} and poleward of 45°S omitted), and daily mean 200-hPa Rossby wave source (magenta contours for positive (anticyclonic vorticity forcing) RWS and black dashed contours for negative (cyclonic vorticity forcing) RWS, interval is 6×10^{-9} s^{-2} from $\pm 30 \times 10^{-9}$ s^{-2} and the zero contour is omitted, see "Methods") for 4 February 2022. **b** Daily anomalies in 500-hPa geopotential height (Z500, gpm; shaded and contoured) and 200-hPa stationary wave flux (vectors, m^2 s^{-2}, with wave fluxes containing zonal components <15 m^2 s^{-2} (easterly or weak westerly) or meridional components >20 m^2 s^{-2} (strongly southerly) omitted; see "Methods") for 4 February 2022. **c**–**h** Same as (**a**, **b**) but for (**c**, **d**) 5 February, (**e**, **f**) 6 February, and (**g**, **h**) 7 February 2022. All anomalies are based on the 1979–2021 long-term mean calculated over the 5-day pentad average centered on each day. Atmospheric data are from ERA5 and OLR data are based on NOAA's interpolated OLR dataset (see "Methods").

February 2022 and from Escudero on 5 and 7 February 2022 (all at 12 UTC) display vertical profiles of temperature associated with anomalously warm troposphere at all levels (in comparison with the last 10 years at Marambio, and the January-February 2022 regular radiosondings for Escudero, Fig. 6a, g). In addition, these profiles show some of the coldest and highest tropopause levels (situated at about 12-km height above sea level compared to the mean tropopause level in summer for this location of around 9 km) (Fig. 6g). For all three profiles, vertical wind shear (S^2, Fig. 6h) develops strong peaks below (5 February, Escudero), above (7 February, Escudero) and at 12 km (7 February, Marambio) followed by strong peaks of enhanced Brünt-Väisälä frequency (N^2, Fig. 6i). This results in Richardson numbers below 10 (Ri, Fig. 6j) and close to critical values for the occurrence of shear turbulence (Ri ~ 0.25[54],) in the whole UTLS. This situation, where dynamic instability (indicated by enhanced S^2) is placed below thermal stability (enhanced N^2, indicative of the stable stratosphere air intrusions) is usually observed within tropopause folds that develop under cyclonic anomalies[55,56]. Under these conditions, strong shear-generated clear-air turbulence is likely to develop[56], both posing risks to aviation over the Drake Passage and influencing tropospheric dynamics and stratospheric ozone levels via enhanced stratosphere-troposphere mixing[57,58].

Comparison with recent AP heatwaves

There were several similar features among the February 2022 hot spell and March 2015 and February 2020 heatwaves. The low-high

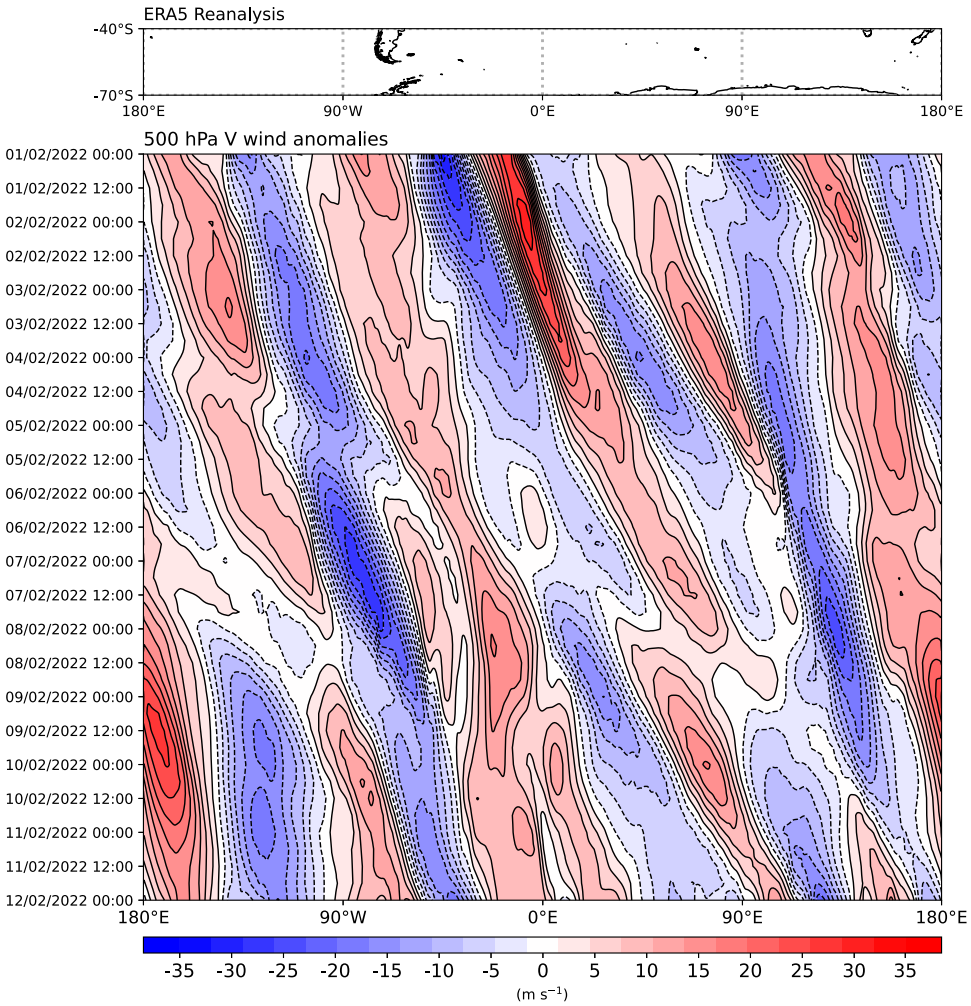

Fig. 8 Rossby wave pattern evolution. Hovmöller diagram (time vs longitude, averaged between the 40°S to 70°S latitudes) of meridional (V) wind anomalies (m s^{-1}, positive northward) at 500-hPa pressure level during 1–12 February 2022. Anomalies are calculated at each time step by subtracting monthly average value during 1979–2022. The box above shows the zonal band over which the averaging was done including the land contours and longitudes matching the diagram. Based on ERA5 reanalysis.

couplet over the Amundsen sea/Drake Passage directing an intense AR towards the AP was key in all three AP extreme warm events (with a strong Amundsen Low anomaly). This couplet shows up clearly in the AR composite fields[26] and it is much stronger than during similar synoptic conditions not associated with ARs[27]. All three major AR events causing extreme high temperatures on the AP were linked to the tropical deep convection. The tropical and subtropical connection was found to characterize major ARs affecting Antarctica, which had strong impacts in terms of either anomalous snowfall or surface melt[33,38].

There were also important differences in the dynamical background among the February 2022 event and previous events. Clem et al.[30,51] showed central tropical convection is an important trigger of stationary Rossby waves in previous AP summer heatwaves. However, the heatwaves in 2015 and 2020 occurred during an El Niño and a neutral ENSO year, respectively, while the February 2022 event occurred during a La Niña. While Clem et al.[29] pointed to a lack of ENSO phase preference for causing central Pacific convection, our results show that both positive SST anomalies and transient mid-latitude activity contributed to additional moisture supply over the SPCZ stretching into the subtropics, where moisture feeding the AR originated. The MJO, which was exceptionally strong in the central tropical Pacific during the March 2015 event[59], was much weaker and confined to the Indian Ocean in February 2022, with negative OLR anomalies west of 90°E. February 2020 is yet another case, during which the MJO was barely detectable above the atmospheric noise. The SAM was positive in February 2022, which favors the presence of a deep Amundsen Sea Low, but wind direction and temperature advection during this case are more consistent with March–May seasonal anomalies rather than December-February for positive SAM[51]. The SAM was also positive during March 2015, and near-neutral during February 2020. Regarding the local drivers, the lee-side of the AP was less affected by foehn warming during the February 2022 event related to a more meridional orientation of the AR impacting the AP compared to the previous heatwaves in March 2015 and February 2020, where the warming signal was much stronger on the leeside and record-high temperatures were observed at Esperanza station (17.5 °C on 24 March 2015 and 18.3 °C on 6 February 2020, while temperature peaked at 7 °C on 7 February 2022)[15,36].

Total accumulated snowmelt and area extent over Larsen C ice shelf was less pronounced during February 2022 compared to February 2020, which still holds the record for surface melt for Larsen C (based on the past 40 years, see Supplementary Fig. 3b, e and ref. [11]). However, February 2022 showed much higher melt values in the northernmost part of the Larsen C and stronger melt over coastal zones of Palmer Land, southern part of Alexander Island and George VI ice shelf (Supplementary Fig. 3c, d). Another distinct feature of the 2022 year is that on 25 February 2022,

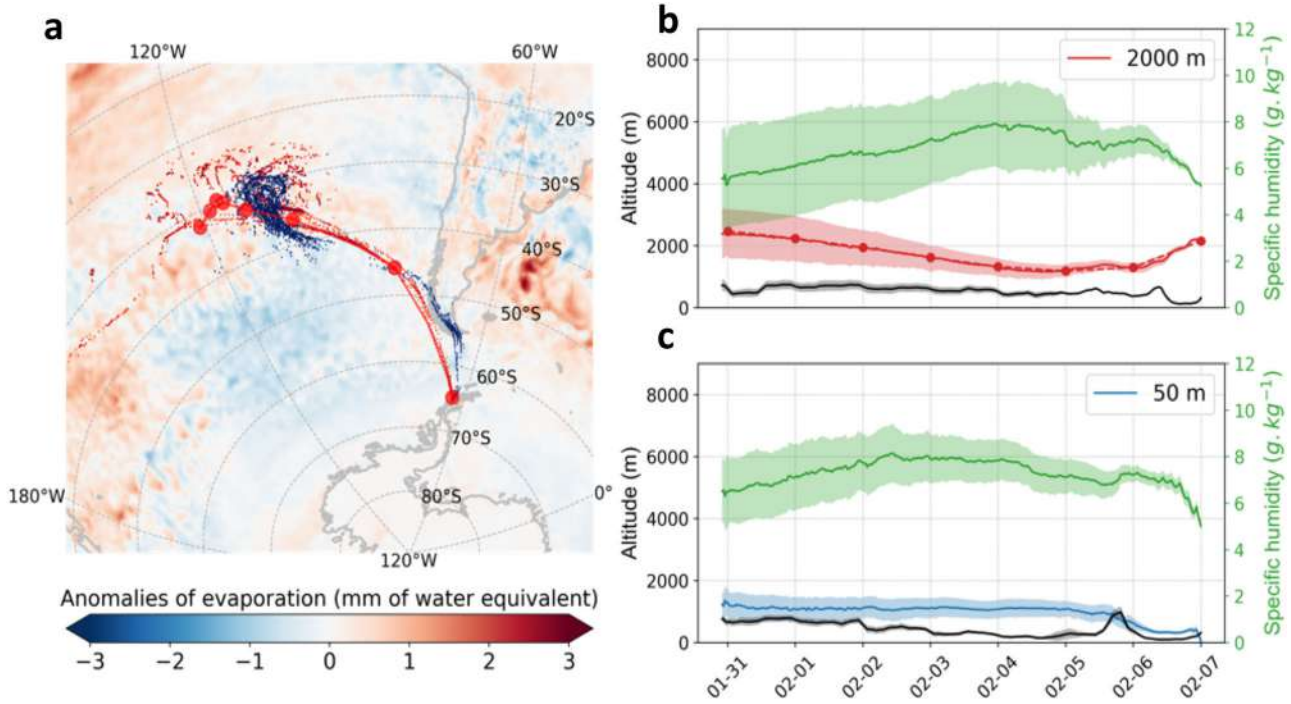

Fig. 9 Surface evaporation and air mass pathways and transformation. a Surface evaporation anomalies (mm w.e., color shading) for February 2022 compared to climatology (1979–2010) and back-trajectories of the air parcels arriving to Vernadsky station on 7 February 2022, 21 UT (near the time of the temperature peak), at the height of 50 m (blue dots) and 2000 m (red dots) with the solid red line indicating the mean trajectory overlaid over the original trajectories for 2000-m height and the circles indicating each day (the mean trajectory for 50-m height are not shown as in this case they are well aligned with the red trajectory). **b** Seven-day back trajectories initiated at the Vernadsky station location on 7 February 2022, 21 UTC at 2000 m height: altitude changes along the trajectory (red line—median, red shading—interquartile range), specific humidity (g/kg, green line—median, green shading—interquartile range) and boundary layer height (black solid line—median, gray shading—interquartile range). **c** Same as (**b**) but for the air parcel trajectories arriving to Vernadsky at the 50 m height (altitude changes along the trajectory shown in blue). Thermodynamic fields are from ERA5. Back-trajectories are calculated using Flexpart model (see "Methods").

sea-ice extent hit its annual minimum at 1.9 million km^2, a record low Antarctic sea-ice extent for the 1979–2022 satellite data[60,61], which has been beaten by a new record low (1.79 million km^2) on 21 February 2023, according to the assessment of the National Atmospheric and Oceanic Administration (NASA) and National Snow and Ice Data Center[62]. Wang et al.[61] emphasized that the Amundsen Sea sea ice loss in February 2022 was more dynamically related, while a strong surface melt contributed to the Weddell Sea sea ice minimum. When the February 2022 event began, there was already no sea ice present in the Bellingshausen Sea, which might have contributed to a deeper southerly inland propagation of the intense AR into the Ellsworth Land in West Antarctica (Fig. 4). The ice-free Bellingshausen Sea may have provided an additional moisture supply to the AR (a small additional increase is visible in specific humidity along the near-surface trajectory when it was near the Vernadsky station, Fig. 9c). The sea ice edge in the northern Weddell Sea moved further south during this AR event and was also probably affected by increased melt.

February 2022 event in the context of climate change

Analysis of summer near-surface air temperatures in the northern AP region (76°–55°W, 62°–70°S, outlined in Fig. 2c) reveals a warming rate of +0.15 °C per decade from 1959 to 2021. To assess how unprecedented the February 2022 event was, we analyzed the event-like analogs—a set of synthetic events constructed by randomly combining the most similar 500-hPa atmospheric circulation analog days in the AP region (see Fig. 2a and "Methods") for each day of the extreme event period—divided into two 31-year periods comparing the temperatures of the recent interval (1991–2021) and a past interval (1960–1990). Results show that the recent period is 0.4 °C warmer with respect to the past period (Fig. 10a), but the 2-day average temperature distribution in the region is only 0.2 °C warmer in the recent period with respect to the past period, which is also consistent with the amplification of the 2020 heatwave[16]. Although the 2-day anomaly of 3.0 °C is not unprecedented in the region since 1959, the probability of reaching this anomaly has increased significantly in the present (96.3 percentile) with respect to the past period (99.8 percentile) (Fig. 10b). However, the similarity of the February 2022 event in both recent and past analogs (indicated by the similar root-mean-square-difference (RMSD), Fig. 10a), indicates that changes in the analog atmospheric circulation are negligible between the two periods reinforcing the role of the thermodynamic warming.

The analysis of the return periods of the 2-m air temperature anomalies for four stations with long-term observations (Rothera, Vernadsky, Esperanza and Marambio, see Fig. 1 and Supplementary Table 1 for station information) reveals that only Vernadsky and Rothera experienced extreme temperatures on 8 February 2022 (Supplementary Table 1). The estimated return period at Vernadsky (maximum of 11.9 °C at 6-h time step) is 116 years. However, for other stations the return periods are much more moderate: the return period at Rothera (with a maximum of 6.5 °C for a 6-h time step) is 1.4 years and the periods at the other three stations are well below 1 year. Using a regional approach over the AP, the 116-year return period experienced in Vernadsky in 2022 turns into a 40-year period at the scale of the AP. This suggests that, despite its obvious strength, a local record of similar

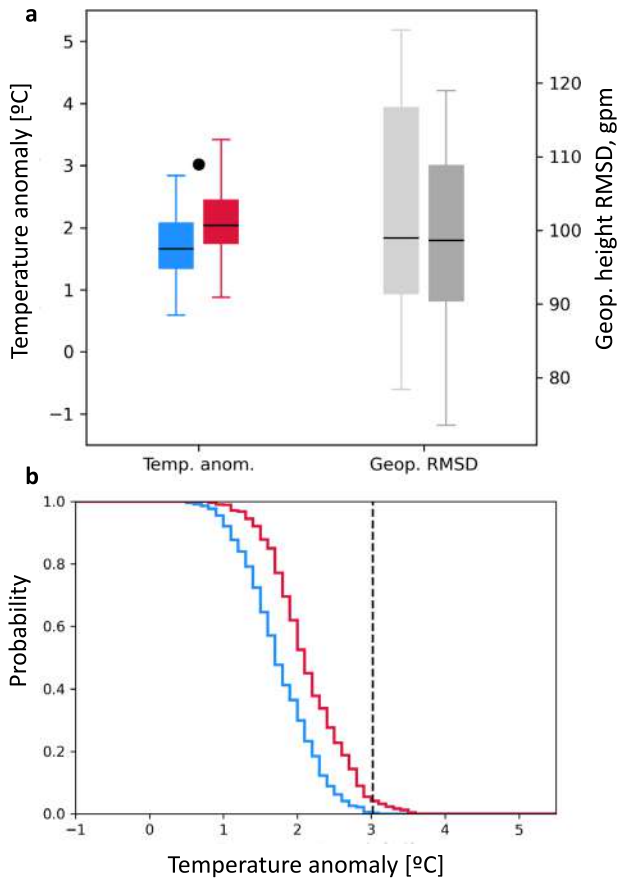

Fig. 10 February 2022 event and atmospheric circulation analogs in climate change. a Analog distribution of the past (1959–1990, blue) and recent (1991–2021, red) 2-day mean near-surface temperature anomalies (°C) averaged over the [62–70°S 76–55°W] region (outlined in Fig. 2d) and 500-hPa geopotential height (gpm) RMSD of the past (light gray) and recent (dark gray) periods in the [55°–78°S, 120–40°W] region (outlined in Fig. 2a). Black lines show medians, boxes indicate the 25th and 75th percentile ranges and whiskers show the 1st–99th percentiles. **b** Cumulative distribution function showing probability of occurrence of temperature anomalies in the past (blue) and recent (red) analogs. Black dot in (**a**) and dashed line in (**b**) indicate the 7 and 8 February 2022 near-surface temperature anomaly. Based on ERA5 reanalysis.

magnitude would not be unlikely at other locations on the AP, especially because anthropogenic global warming is already expected to amplify temperature extremes there[16]. This is confirmed by the occurrence of the highest recent records at the Esperanza station in 2015 and 2020.

The AR that brought this hot spell in early February 2022 followed several weather systems including ARs of smaller intensities during the summer, which influenced regional sea ice, including the anomalously low sea ice in the Bellingshausen Sea[60,61]. The record-high surface melt, together with anomalously low sea-ice extent in the Bellingshausen Sea in February 2022 (Supplementary Fig. 11b) that was then followed by another intensive melt and sea ice record low in February 2023, have likely contributed to a series of small ice loss events from Wilkins ice shelf and further increased the fragility of Larsen C ice shelf[62]. Moreover, in late January 2022, a large expanse of land-fast ice (about 2000 km^2), which was present in the Larsen B embayment since 2011, disintegrated over a few days and the embayment was almost completely clear of sea ice on 8 February (according to the NASA Earth Observatory images[63]). The 7–9 February event was part of a series of ARs (starting in late January) triggering strong foehn winds and large ocean swells that likely played a major role in this Larsen B embayment fast-ice breakout[63]).

DISCUSSION

On 7 and 8 February 2022, the AP experienced extremely high temperatures (breaking absolute maximum temperature records at several stations) and record high short-period surface melt compared to the previous 43 years. The widespread surface melt affected both the western and eastern sides of the AP including both Wilkins, George VI and Larsen C ice shelves (based on the estimates from satellite observations and the regional climate model MAR). Both the northwestern and northern AP were directly impacted by the AR, which brought extreme high temperatures and rainfall, while the foehn effect and increased net shortwave flux during cloud clearance were the main source of warming in the northeastern leeward side. Both the hot spell and peak surface melt on the AP were related to the anomalous deep convection event that occurred in the central tropical Pacific and SPCZ, together with background La Niña conditions including warm SST anomalies concentrated in subtropical western and central parts of the southern Pacific. These tropical convection anomalies likely served as a trigger for the stationary Rossby wave flux propagation towards the AP that then contributed to the development of anomalously strong low-level cyclonic and anticyclonic anomalies around the AP and Rossby wave breaking during the AP hot spell event. The AR, which brought warm and moist anomalies to the AP, had a high intensity (reaching AR scale 3 with extremely high IWV at the AP) and drew its moisture from the subtropical South Pacific Ocean, where anomalously warm SSTs and evaporation occurred. The AR was channeled in a more meridional direction towards the AP (compared to previous ARs associated with heatwaves in February 2020 and March 2015) by record-high values of the ridge in the Weddell Sea and anomalously low values of the Amundsen-Sea Low. The large affected area and several extreme parameters affecting the same region make it a multivariate and spatial compound event.

This extreme weather event brought significant precipitation and strong winds that had major impacts on local operations. Flights from Punta Arenas (Chile) to King George Island were canceled first due to strong cross-winds and later due to low stratus clouds and fog, generating a series of disruptions in the logistics chain, especially for scientific transport. In addition, scientific vessels had to postpone travel, also affecting the supply of stations and stranding personnel during the field campaigns. This series of disruptions delayed and shortened scientific projects. Such events also pose difficulties for operational forecasts, which frequently underestimate their magnitude. Moreover, we showed association of this extreme event with increased upper-troposphere turbulence, which can pose risk to aviation over the Drake Passage. The February 2022 AR event and most recent extreme weather events illustrate the need to further develop and improve operational forecasting tools for Antarctica in a coordinated effort, such as the Year of Polar Prediction in the Southern Hemisphere[64].

The AP has undergone one of the most rapid regional warmings in the world[3–5]. Global and regional climate models project an increase in near-surface temperatures across the entire Antarctic[5,65] and particularly over the AP in the next two decades[66]. CMIP6 model future projections show both mean and maximum temperatures progressively increasing with future global warming (Supplementary Fig. 12, refs. [5,67]). At the same time, these models continue to poorly reproduce extremes in statistical distributions and they require further process-based evaluation and improvement. To overcome these limitations, the atmospheric circulation analog method used here has the advantage of relying on observational based products and provides a way to assess the thermodynamic response to climate change, without introducing

the uncertainty of the dynamical response[68]. Furthermore, these results suggest that the event may have been amplified by global warming with higher probability of occurrence during the most recent period (1991–2022) compared to 1959–1990, in agreement with results from analysis of the heatwave of February 2020[16]. The most recent extreme warm events over the AP add increasing evidence to recent studies that suggest that heatwaves will be more frequent in a warmer world[9,67]. However, improved understanding and further analysis of the exact mechanisms (thermodynamic or dynamical changes) that underlay these extremes are still needed.

These extreme warm events, which may be inconsequential in terms of meltwater production for most of Antarctica, can lead to widespread melt intensification on the Antarctic Peninsula, where the surface temperature is much closer to 0 °C year-round but particularly in summer[66]. In response to rising temperatures and increased frequency of warm episodes, surface melt is projected to significantly increase in upcoming decades regardless of the emission scenario[45,67,69]. Although the impact of such extreme warm events and the associated enhanced surface melt is not expected to become large in terms of ice-sheet mass balance, it may lead to lasting and larger meltwater ponds. On an ice shelf, meltwater can fill and magnify ice crevasses, weakening the ice shelf stability, which was found to play an important role (among other factors) in earlier AP ice shelf disintegrations[70] and has been evaluated as a danger for the Larsen C ice shelf[13,45]. Thus, understanding the processes and impacts of these extreme temperature events associated with atmospheric rivers is of high importance for future Antarctic and global sea level projections.

METHODS

Ground-based temperature and precipitation observations

Station records of 2-m air temperatures (Fig. 2d, e, Supplementary Fig. 1, and Supplementary Table 1) are measured by automatic weather stations (AWS) during different periods at each AP station used in the study. Station locations, measurement periods and operating countries/institutions are provided in Supplementary Table 1. See "Data availability" section for data sources.

The precipitation measurements were carried out using the Frequency-Modulated Continuous-Wave (FM-CW) 24-GHz Doppler micro rain radar (MRR-PRO) deployed at the Vernadsky station with a temporal resolution of 30 s. The MRR-PRO provides vertical profiles of equivalent reflectivity (Ze), which can be converted into precipitation rate (R) using the power law relationship between Ze and R. Here, only the precipitation in the form of rainfall was analyzed using the MRR-PRO, during the 7 and 8 of February, where the melting layer was located approximately at 2.5 km a.s.l. (according to the MRR-PRO Doppler moments). The $Ze = 200R^{1.6}$ relationship developed by Marshall and Palmer (1948) was used to estimate rainfall rate at Vernadsky during the event (replacing the manufacturer product, which showed unrealistic precipitation values).

ERA5 reanalysis fields

The European Centre for Medium-Range Weather Forecasts (ECMWF) ERA5 reanalysis was used for synoptic and climatological analyses with the data on surface, pressure and isentropic levels[71]. ERA5 reanalysis uses IFS model CY45R1 and provides hourly output variables based on ~30-km horizontal resolution and 137 vertical levels. Here the data from 1959 to 2022 are used.

Integrated vapor transport (***IVT***, kg m^{-1} s^{-1}) is calculated using ERA5 data as

$$\boldsymbol{IVT} = -\frac{1}{g}\left\langle \sum_{k=1}^{300\,\mathrm{hPa}} u_k q_k \Delta p_k, \sum_{k=1}^{300\,\mathrm{hPa}} v_k q_k \Delta p_k \right\rangle \quad (1)$$

where index k corresponds to the pressure levels from surface ($k = 1$) to 300 hPa, Δp_k is the difference in pressure (Pa) between the levels, u and v (m s^{-1}) are zonal and meridional wind components, respectively, q (kg kg^{-1}) is specific humidity, and g (m s^{-2}) is gravitational acceleration. Integrated water vapor (IWV) is calculated by integrating specific humidity for the same pressure levels and boundaries.

The AR scale is calculated following Ralph et al.[46] and is based on the IVT intensity and duration at a given grid point (here we used ERA5 reanalysis). AR categories are defined using minimum thresholds for the maximum instantaneous IVT during the period of AR conditions of 250, 500, 750, 1000, and 1250 kg m^{-1} s^{-1}, and the duration of the defined AR conditions at each point (24, 48 and 72 h).

We also use snow melt product from the ERA5 Land reanalysis with ~9 km (0.1 degree) horizontal resolution. ERA5-Land uses the Carbon Hydrology-tiled ECMWF Scheme for Surface Exchanges over Land (CH-TESSEL) for computing the snow depth[72]. It is initialized with a glacier mask to better represent the glacier spatial distribution.

Circulation analogs

Analogs and anomalies and percentile maps have been calculated using summer (DJF) daily averages of 2-m temperature and geopotential height at 500 hPa every 6 h in ERA5 reanalysis at 0.5° horizontal resolution. Two-day anomalies and percentiles were calculated with respect to the two consecutive daily average climatology from 1959 to 2021. Circulation analogs for the two event days were calculated using the 500-hPa geopotential height over the [55°–78°S; 120–40°W] region (Fig. 2a) and identified as the 20 days with the lowest Root Mean Square Difference (RMSD) in the past (1959–1990) and recent (1991–2021) sub-periods, separately, where RMSD is defined as:

$$\mathrm{RMSD} = \sqrt{\frac{\sum_i^n \left(Z500_i^{\mathrm{Analog}} - Z500_i^{\mathrm{Clim}}\right)^2}{n}} \quad (2)$$

where i is each of the n grid points in the [55°–78°S; 120–40°W] region (see the region contours in Fig. 2a) and $Z500_i^{\mathrm{Analog}}$ and $Z500_i^{\mathrm{Clim}}$ correspond to the 500-hPa geopotential height at the grid point in the analog and climatology (after weighting by the square root of the cosine of the latitude). 2-m air temperature anomalies for each of the analog days were calculated using the [62–70°S 76–55°W] region centered in the northern AP (see the region contours in Fig. 2c). Analog-like temperature events were reconstructed by picking randomly one of the analog days for each event day and combining them. This process was repeated $N = 5000$ times producing circulation-constrained temperature distributions for the past and recent sub-periods (more details can be found in ref. [16]).

Regional climate model MAR

The MAR model ("Modèle Atmosphérique Régional" in French) is a polar-oriented regional climate model extensively used to study the Antarctic ice sheet climate and surface mass balance and described in detail by refs. [69,73]. In this study, we use MARv3.12, with the improvements introduced by ref. [74] concerning the snow model, including a better representation of snow temperature at the base of the modeled snowpack and continuous conversion from rainfall to snowfall from 0 °C to −2 °C as the snow model input. For this study, the MAR snow model resolves the first 20 m of the snowpack into 30 layers of varying thickness and its starting conditions are interpolated from the previous simulation performed by ref. [69]. MAR was run with a 7.5 km spatial resolution over the AP from 1980 to 2022, forced at the lateral boundaries and over the ocean by the 6-hourly ERA5 reanalysis[71]. The

Antarctic topography, land-ice-ocean mask, and ice shelf extent used in the MAR run for this study are based on the surface digital elevation model REMA - Reference Elevation Model of Antarctica[75], as part of the MEaSUREs BedMachine Antarctica (see data availability). The MARv3.12 model evaluation using AWS around the Antarctic ice sheet showed that the model represents well the near-surface meteorology and radiative fluxes, while slightly overestimating some peaks of surface melt (which can be due to a difference in altitude between MAR surface and the AWS)[76].

Snowmelt from models and satellite observations

The amount and/or extent of snowmelt during February 2022 (Fig. 3d, e) was analyzed using three different products: (1) the ERA5-Land reanalysis product (described above); (2) outputs from the regional climate model MAR; and 3) dry/wet snow status product derived from microwave satellite observations.

The maximum daily extent from ERA5-land and MAR model was compared to the product derived from the satellite observations —the 12.5-km resolution dry/wet snow status product derived combining the 19-GHz Advanced Microwave Scanning Radiometer - Earth Observing System (AMSR-E) satellite between 2003 and 2011 and its successor AMSR-2 between 2013 and 2023[77]. The passive microwave satellite observations can detect liquid water within the snowpack, based on the changes of brightness temperature (TB), because wet snow has a significantly larger emissivity than dry snow[78]. The dry/wet snow status product was produced using TB from the ascending (13h30 local time) and descending (01h30 local time) orbits of AMSR-E and AMSR-2 and an algorithm developed by refs. [78,79].

All datasets were converted into the Lambert Azimuthal Equal Area projection to compute the maximal melt extent in the Antarctic Peninsula during every February since 1980. For the case of ERA5-Land and MAR, maximum daily extents of melt were calculated using the respective accumulated snowmelt products. To avoid over classification of melting grid points, two different minimum snowmelt thresholds (0.1 and 1 mm w.e. day^{-1}) were considered to determine if a grid point corresponds to dry or melting snow. The maximum daily extent of melt relative to the AP surface was estimated during February in 2020 and 2022 (see Supplementary Table 2), using the snowmelt extents from the MAR model, satellite observations (AMSR-2) and ERA5-Land reanalysis data presented in Fig. 3e and the AP surface estimated at the resolution of each product within the area defined by the extent of the MAR model north of −75° latitude (see Fig. 1, red line).

Polar WRF model

The local analysis presented in Fig. 4 is based on the high-resolution Polar WRF (version 4.3.3) simulations output using 3-domain downscaling with 30-, 6-, and 1.2-km spatial resolution. It included advanced configuration most suitable for the AP foehn and cloud radiative forcing processes representation, including two-moment cloud microphysics scheme (Morrison–Milbrandt P3 scheme), Rapid Radiative Transfer Model, Kain-Fritsch scheme for cumulus parameterization, and Noah-MP for the land surface model. The Morrison-Milbrandt P3 scheme considers the particle properties for clouds as continuum, in contrast with other microphysics parameterization scheme, showing a better performance in the estimation of the liquid water path[43]. The model setup used in this study is described in detail by Zou et al.[43] and references therein. Polar WRF topography information is based on the 1-km Reference Elevation Model of Antarctica (REMA)[75]. Here we used output from the 1.2-km spatial resolution domain. Model evaluation using AWS and radiosonde measurements at several AP stations showed reasonably good performance of the Polar WRF (high resolution domain) with respect to the surface pressure, wind speed and temperature, despite some negative bias in temperature[43].

Vertical profiles from radiosondes and ERA5

During the event, balloon-borne GRAW radiosondes (model DFM-09), fitted with a pressure microsensor, were launched from Escudero (Fig. 6 and Supplementary Fig. 4). The radiosondes measured the vertical distribution of temperature, relative humidity, pressure, and winds up to about 20 km. Zonal, meridional and total moisture fluxes (kg kg^{-1} m s^{-1}) were calculated as qu, qv, and qWS, respectively, where q is specific humidity (kg kg^{-1}), u and v are zonal and meridional wind speeds, respectively, and WS is measured wind speed. For the profiles in Fig. 6g–j, raw data (temperature, wind speed, pressure) from Marambio (Väisälä RS41 radiosonde) and Escudero (GRAW-DF09) radiosonde launches were used. After two smoothing steps (first, taking a 10-point vertical mean and then using cubic splines), the raw data are used to derive temperature and velocity derivatives. Further, we calculated the profiles of the squared vertical wind shear S^2, the squared Brunt–Väisälä frequency N^2, and the Richardson number Ri, as following:

$$N^2 = \frac{g}{\theta}\frac{\partial\theta}{\partial z} \tag{3}$$

$$\mathrm{Ri} = \frac{N^2}{S^2},\ \text{where } S^2 = \left(\frac{\partial u}{\partial z}\right)^2 + \left(\frac{\partial v}{\partial z}\right)^2 \tag{4}$$

where θ is the smoothed potential temperature, g is the gravitational acceleration, and u and v are the zonal and meridional wind components, respectively. All these parameters were calculated using a centered-in-space finite differences scheme. We use the threshold of Richardson number below the critical value of $\mathrm{Ri_c} = 0.25$, as favorable conditions for the occurrence of turbulence. It is worth noticing that due to this data selection process, for radiosonde data for Escudero station on 5 February smoothing procedures leave insufficient points to obtain information on S^2 and N^2 above 12 km. Also note that derived values of Ri numbers diverge at some points. This is because S^2 can reach very small values in some places, and is why the vertical profile of Ri for radiosonde data for Marambio on February 5 are not displayed. For more details, see ref. [56].

Tropical convection and Rossby wave analysis

Several daily-mean fields from ERA5 were used to investigate anomalies in the atmospheric circulation shown in Fig. 7, including divergent wind, horizontal stationary wave flux and Rossby wave source at 200 hPa (based on the formulations of refs. [80–82] detailed below) and 500-hPa geopotential height. Patterns of anomalous deep convection were investigated using daily-mean outgoing longwave radiation (OLR) from the NOAA Interpolated OLR dataset[83] on a 2.5° × 2.5° latitude–longitude grid. Daily anomalies were calculated based on the 1979–2021 long-term mean for each day, defined here as the long-term mean of the 5-day pentad mean centered on each day (i.e., the 6 February 2022 anomalies are based on the 4–8 February mean climatology).

The zonal ($\boldsymbol{W}x$) and meridional ($\boldsymbol{W}y$) components of the stationary wave[81] shown in Fig. 7 take the form:

$$\boldsymbol{W}x = \frac{p\cos(\phi)}{2|\mathbf{U}|}\left[\frac{\overline{U}}{a^2\cos^2(\phi)}\left(\left(\frac{\partial\psi}{\partial\lambda}\right)^2 - \psi\frac{\partial^2\psi}{\partial\lambda^2}\right) + \frac{\overline{V}}{a^2\cos(\phi)}\left(\frac{\partial\psi}{\partial\lambda}\frac{\partial\psi}{\partial\phi} - \psi\frac{\partial^2\psi}{\partial\lambda\partial\phi}\right)\right] \tag{5}$$

$$\boldsymbol{W}y = \frac{p\cos(\phi)}{2|\mathbf{U}|}\left[\frac{\overline{U}}{a^2\cos(\phi)}\left(\frac{\partial\psi}{\partial\lambda}\frac{\partial\psi}{\partial\phi} - \psi\frac{\partial^2\psi}{\partial\lambda\partial\phi}\right) + \frac{\overline{V}}{a^2}\left(\left(\frac{\partial\psi}{\partial\phi}\right)^2 - \psi\frac{\partial^2\psi}{\partial\phi^2}\right)\right] \tag{6}$$

where λ and ϕ are the longitude and latitude coordinates, respectively, ψ is the geostrophic streamfunction anomaly, $\overline{U}$ and $\overline{V}$ are the mean climatological zonal and meridional winds, respectively, $|\mathbf{U}|$ is the magnitude of the climatological horizontal

winds, p is the normalized pressure, which is the pressure divided by a standard reference pressure of 1000 hPa, and a is the radius of the Earth. Defined in this fashion, the fluxes indicate the direction of anomalous horizontal stationary Rossby wave propagation[80,81].

The low-level convergence and upper-level divergence associated with enhanced tropical convection generates an anomalous vorticity source that can generate Rossby waves. To examine the vorticity forcing of Rossby waves associated with tropical convection we use the Rossby wave source (RWS) at 200 hPa, which is calculated following ref. [82] based on the barotropic vorticity equation:

$$\mathrm{RWS} = -\mathbf{V}_\chi \nabla(\zeta + f) - \boldsymbol{D}(\zeta + f) \tag{7}$$

where $\mathbf{V}_\chi$ is the divergent component of the horizontal wind at 200 hPa, $\boldsymbol{D}$ is horizontal divergence at 200 hPa, and $\zeta + f$ is the relative vorticity and Coriolis parameter, respectively; the sum of ζ and f equals absolute vorticity. The first term of the RWS $[-\mathbf{V}_\chi \nabla(\zeta + f)]$ is the advection of absolute vorticity by the divergent wind, and the second term $[\boldsymbol{D}(\zeta + f)]$ is the generation of absolute vorticity through vortex stretching. In Fig. 7, the RWS is examined to diagnose the Rossby wave dynamics associated with anomalous convection in the central tropical Pacific, whereby positive and negative RWS values generate anticyclonic and cyclonic vorticity tendencies, respectively, in the Southern Hemisphere.

Moisture sources and pathways from back trajectories with ERA5

The trajectories of the air parcels (Fig. 9) reaching the northern AP (at the location of Vernadsky station) were calculated using FLEXPART (version 10.4[84]), which is a Lagrangian particle dispersion model (forced with meteorological data from ERA5 at $1° \times 1°$ horizontal resolution). Every 6 h, 500 neutral inert air tracer particles are randomly placed in a volume ($0.1° \times 0.1° \times 100$ m) centered around the selected AP stations coordinates at designated altitudes (ranging from 50 m to 3050 m) and then released over a 3-hour window (around 83 particles every 30 min) to compute 10-day back-trajectories. This allows us to construct 3-D position of the air parcels evolving in time at a 30-minute time resolution on a 0.25°x0.25° horizontal grid. For each air parcel and for each time step, key variables (such as specific humidity and boundary layer height used in this study) are extracted from ERA5 by FLEXPART, giving the state of the atmosphere at the parcel positions.

Long-term temperature statistics

Temperature data from different stations from the AP were analyzed here to estimate the return period of February 8, 2022 event across the AP. Data from Rothera, Vernadsky, Esperanza and Marambio stations were studied here (see Supplementary Table 1 for the station coordinates and measurement periods). Instantaneous temperature is available at these stations every 6 h. Daily maxima (Tmax) were computed based on the 6-h mean values, to assess the return periods of the event. We also computed the return time values of temperature anomalies by subtracting the daily averages over the whole period from the daily values. Estimations follow the Extreme Value Theory[85] which states that peaks over a large threshold can be modeled by the Generalized Pareto Distribution (GPD) whose cumulative distribution function is given by:

$$F_{(\mu,\sigma,\xi)}(T) = 1 - \left(1 + \frac{\xi(T-\mu)}{\sigma}\right)^{-\frac{1}{\xi}} \tag{8}$$

for any temperature T exceeding the large threshold μ. The GPD scale ($\sigma > 0$) and shape ($\xi \in R$) parameters model respectively the variability and the tail-heaviness of the peaks. In this study, the threshold μ is set to the 99th percentile, so on average about 3 exceedances per year are considered at each station. The analysis was also performed with a 98th percentile, giving very similar results. The GPD parameters (σ,ξ) are estimated at each station by maximum likelihood method. The return period (RP) of a given extreme temperature T (exceeding μ) is calculated as in ref. [85]:

$$\mathrm{RP}(T) = \frac{1}{n \times p \times (1 - F_{(\mu,\sigma,\xi)}(T))} \tag{9}$$

where $n = 365.25$ and $p = 1$–0.99. Confidence intervals are obtained by parametric bootstrap drawing 500 GPD samples at each station.

DATA AVAILABILITY

ERA5 and ERA5-Land data are available via ECMWF Copernicus Climate Change Service (C3S, https://cds.climate.copernicus.eu). Station data availability: Gabriel de Castilla, Juan Carlos I station data are provided by the Antarctic Group, Spanish Meteorological Agency (AEMET); Vernadsky data from meteorological station Troposphera are available at http://dskiev.com.ua/oborudovanie_troposfera.html and Vaisala AWS data are available upon request; Escudero data are provided by University of Chile, Antarctic group, and available upon request; Eduardo Frei Montalva data are provided by the Chilean Weather Service (DMC, https://climatologia.meteochile.gob.cl/) and available upon request; King Sejong data are provided by the Korea Polar Research Institute (KOPRI) and available at https://dx.doi.org/doi:10.22663/KOPRI-KPDC-00001987.2; Carlini, Marambio, Esperanza, San Martin stations are operated by Servicio Meteorológico Nacional (SMN) and Dirección Nacional del Antarctico (DNA), Argentina, and data are available upon request to CIM-SMN: cim@smn.gov.ar; Palmer data are available at https://amrc.ssec.wisc.edu/usap/palmer and http://amrc.ssec.wisc.edu/data/ftp/pub/palmer/climatology/ (provided by Marissa Goerke, the Palmer Station Research Associate). We also used station and AWS data available at SCAR-READER (https://legacy.bas.ac.uk/met/READER/ANTARCTIC_METEOROLOGICAL_DATA/) and Antarctic Meteorological Research and Data Center (AMRDC) Data Repository database (https://doi.org/10.48567/1hn2-nw60). Antarctic Satellite Composite Imagery is made available via the AMRDC Data Repository (https://doi.org/10.48567/cfxm-4c37). The snow status derived from passive microwave radiometers during 2002–2023 is available at https://perscido.univ-grenoble-alpes.fr/datasets/DS391. The digital elevation model REMA used in MARv3.12 is available via MEaSUREs BedMachine Antarctica, v.3 dataset, NASA National Snow and Ice Data Center Distributed Active Archive Center (https://doi.org/10.5067/FPSU0V1MWUB6). The REMA topography used in Polar WRF simulations is based on Gerber, F. and Lehning, M.: REMA topography and AntarcticaLC2000 for WRF. EnviDat. doi:10.16904/envidat.190. (2020). Polar WRF and MAR output data used in this study are available upon demand.

CODE AVAILABILITY

All codes used in this study are available upon request. The MAR code used in this study is tagged as v3.12 on https://gitlab.com/Mar-Group/MARv3 (MAR model, 2022). The Polar WRF source code can be requested via https://polarmet.osu.edu/PWRF/registration.php. Codes for analog calculations follow Gonzalez-Herrero et al. (2022) methodology available in Github repository: https://github.com/sergigonzalezh/2020AntarcticHeatwave_attribution_analogs.

Received: 2 February 2023; Accepted: 17 November 2023;
Published online: 04 December 2023

REFERENCES

1. Masson-Delmotte, V. et al. (eds) *IPCC: Climate Change 2021: The Physical Science Basis. Contribution of Working Group I to the Sixth Assessment Report of the Intergovernmental Panel on Climate Change* (Cambridge University Press, 2021).
2. WMO. World Meteorological Organization press release, No 19012022. https://wmo.int/media/news/2021-one-of-seven-warmest-years-record-wmo-consolidated-data-shows (2022).
3. Jones, M. E. et al. Sixty years of widespread warming in the southern middle and high latitudes (1957–2016). *J. Clim.* **32**, 6875–6898 (2019).
4. Turner, J. et al. Antarctic temperature variability and change from station data. *Int. J. Climatol.* **40**, 2986–3007 (2019).
5. Gutiérrez, J. M. et al. in *Climate Change 2021: The Physical Science Basis. Contribution of Working Group I to the Sixth Assessment Report of the Intergovernmental Panel on Climate Change* 1927–2058 (Cambridge University Press, 2021).

6. Gonzalez, S. & Fortuny, D. How robust are the temperature trends on the Antarctic Peninsula? *Ant. Sci.* **30**, 322–328 (2018).
7. Bozkurt, D. et al. Recent near-surface temperature trends in the Antarctic Peninsula from observed, reanalysis and regional climate model data. *Adv. Atmos. Sci.* **37**, 477–493 (2020).
8. Carrasco, J. F., Bozkurt, D. & Cordero, R. R. A review of the observed air temperature in the Antarctic Peninsula. Did the warming trend come back after the early 21st hiatus? *Polar Sci.* **28**, 100653 (2021).
9. Seneviratne, S. I. et al. in *Climate Change 2021: The Physical Science Basis* Ch. 11 (Contribution of Working Group I to the Sixth Assessment Report of the Intergovernmental Panel on Climate Change, Cambridge University Press, 2021).
10. Turner, J. et al. Extreme temperatures in the Antarctic. *J. Clim.* **34**, 2653–2668 (2021).
11. Bevan, S., Luckman, A., Hendon, H., Wang, G. & Larsen, C. Ice Shelf surface melt is a 40-year record high. *Cryosphere* **14**, 3551–3564 (2020).
12. Banwell, A. F. et al. The 32-year record-high surface melt in 2019/2020 on the northern George VI Ice Shelf, Antarctic Peninsula. *Cryosphere* **15**, 909–925 (2021).
13. Gilbert, E., Orr, A., King, J. C., Renfrew, I. A. & Lachlan-Cope, T. A 20-year study of melt processes over Larsen C ice shelf using a high-resolution regional atmospheric model: 1. Model configuration and validation. *J. Geophys. Res. Atmos.* **127**, e2021JD034766 (2022).
14. Francelino, M. R. et al. WMO evaluation of two extreme high temperatures occurring in February 2020 for the Antarctic Peninsula region. *Bull. Am. Meteorol. Soc.* **102**, E2053–E2061 (2021).
15. Xu, M. et al. Dominant role of vertical air flows in the unprecedented warming on the Antarctic Peninsula in February 2020. *Commun. Earth Environ.* **2**, 133 (2021).
16. González-Herrero, S., Barriopedro, D., Trigo, R. M., Lopez-Bustins, J. A. & Oliva, M. Climate warming amplified the 2020 record-breaking heatwave in the Antarctic Peninsula. *Commun. Earth Environ.* **3**, 122 (2022).
17. Krakovska, S. Meteorological records and analysis of the temperature regime of the Faraday-Vernadsky station. *Bull. Ukrainian Antarctic Center* **2**, 64–69 (1998).
18. Uotila, P., Vihma, T. & Tsukernik, M. Close interactions between the Antarctic cyclone budget and large-scale atmospheric circulation. *Geophys. Res. Lett.* **40**, 3237–3241 (2013).
19. Papritz, L. et al. The role of extratropical cyclones and fronts for Southern Ocean freshwater fluxes. *J. Clim.* **27**, 6205–6224 (2014).
20. Grieger, J., Leckebusch, G. C., Raible, C. C., Rudeva, I. & Simmonds, I. Subantarctic cyclones identified by 14 tracking methods, and their role for moisture transports into the continent. *Tellus A Dyn. Meteorol. Oceanogr.* **70**, 1–18 (2018).
21. Sinclair, M. R. A climatology of anticyclones and blocking for the Southern Hemisphere. *Mon. Weather Rev.* **124**, 245–264 (1996).
22. Massom, R. A. et al. Precipitation over the Interior East Antarctic Ice Sheet related to midlatitude blocking-high activity. *J. Clim.* **17**, 1914–1928 (2004).
23. Hirasawa, N., Nakamura, H., Motoyama, H., Hayashi, M. & Yamanouchi, T. The role of synoptic-scale features and advection in pro- longed warming and generation of different forms of precipitation at Dome Fuji station, Antarctica, following a prominent blocking event. *J. Geophys. Res. Atmos.* **118**, 6916–6928 (2013).
24. Schlosser, E. et al. Characteristics of high-precipitation events in Dronning Maud Land, Antarctica. *J. Geophys. Res. Atmos.* **115**, D14107 (2010).
25. Gorodetskaya, I. V. et al. The role of atmospheric rivers in anomalous snow accumulation in East Antarctica. *Geophys. Res. Lett.* **41**, 6199–6206 (2014).
26. Wille, J. D. et al. Antarctic atmospheric river climatology and precipitation impacts. *J. Geophys. Res. Atmos.* **126**, e2020JD033788 (2021).
27. Pohl, B. et al. Relationship between weather regimes and atmospheric rivers in East Antarctica. *J. Geophys. Res.* **126**, e2021JD035294 (2021).
28. Bozkurt, D., Marín, J. C. & Barrett, B. S. Temperature and moisture transport during atmospheric blocking patterns around the Antarctic Peninsula. *Weather Clim. Extrem.* **38**, 100506 (2022)
29. Clem, K. R., Bozkurt, D., Kennett, D., King, J. C. & Turner, J. Central tropical Pacific convection drives extreme high temperatures and surface melt on the Larsen C Ice Shelf, Antarctic Peninsula. *Nat. Commun.* **13**, 3906 (2022).
30. Ralph,, F. M., Neiman, P. J. & Wick, G. A. Satellite and CALJET aircraft observations of atmospheric rivers over the eastern North Pacific Ocean during the winter of 1997/98. *Mon. Weather Rev.* **132**, 1721–1745 (2004).
31. Sodemann, H. & Stohl, A. Moisture origin and meridional transport in atmospheric rivers and their association with multiple cyclones. *Mon. Weather Rev.* **141**, 2850–2868 (2013).
32. Dacre, H. F., Martínez-Alvarado, O. & Mbengue, C. O. Linking atmospheric rivers and warm conveyor belt airflows. *J. Hydrometeorol.* **20**, 1183–1196 (2019).
33. Terpstra, A., Gorodetskaya, I. V. & Sodemann, H. Linking sub-tropical evaporation and extreme precipitation over East Antarctica: an atmospheric river case study. *J. Geophys. Res. Atmos.* **126**, e2020JD033617 (2021).
34. Gorodetskaya, I. V., Silva, T., Schmithüsen, H. & Hirasawa, N. Atmospheric river signatures in radiosonde profiles and reanalyses at the Dronning Maud Land Coast, East Antarctica. *Adv. Atmos. Sci.* **37**, 455–476 (2020).
35. González-Herrero, S. et al. Extreme precipitation records in Antarctica. *Int. J. Climatol.* **43**, 3125–3138 (2023).
36. Bozkurt, D., Rondanelli, R., Marin, J. C. & Garreaud, R. Foehn event triggered by an atmospheric river underlies record-setting temperature along continental Antarctica. *J. Geophys. Res Atmos.* **123**, 3871–3892 (2018).
37. Wille, J. D. et al. West Antarctic surface melt triggered by atmospheric rivers. *Nat. Geosci.* **12**, 911–916 (2019).
38. Wille, J. D. et al. Intense atmospheric rivers can weaken ice shelf stability at the Antarctic Peninsula. *Commun. Earth Environ.* **3**, 90 (2022).
39. Francis, D., Mattingly, K. S., Temimi, M., Massom, R. & Heil, P. On the crucial role of atmospheric rivers in the two major Weddell Polynya events in 1973 and 2017 in Antarctica. *Sci. Adv.* **6**, eabc2695 (2020).
40. Teubler, F. & Riemer, M. Potential-vorticity dynamics of troughs and ridges within Rossby wave packets during a 40-year reanalysis period. *Weather Clim. Dyn.* **2**, 535–559 (2021).
41. Wirth, V. & Eichhorn, J. Long-lived Rossby wave trains as precursors to strong winter cyclones over Europe. *Q. J. R. Meteorol. Soc.* **680**, 729–737 (2014).
42. Lavaysse, C. et al. Towards a monitoring system of temperature extremes in Europe. *Nat. Hazards Earth Syst. Sci.* **18**, 91–104 (2018).
43. Zou, X. et al. Strong warming over the Antarctic Peninsula during combined atmospheric river and foehn events: contribution of shortwave radiation and turbulence. *J. Geophys. Res. Atmos.* **128**, e2022JD038138 (2023).
44. Scambos, T. A. et al. Ice shelf disintegration by plate bending and hydro-fracture: Satellite observations and model results of the 2008 Wilkins ice shelf break-ups. *Earth Planet. Sci. Lett.* **280**, 51–60 (2009).
45. Gilbert, E. & Kittel, C. Surface melt and runoff on Antarctic ice shelves at 1.5 °C, 2 °C, and 4 °C of future warming. *Geophys. Res. Lett.* **48**, e2020GL091733 (2021).
46. Ralph, F. M. et al. A scale to characterize the strength and impacts of atmospheric rivers. *Bull. Am. Meteorol. Soc.* **100**, 269–289 (2019).
47. Zscheischler, J. et al. A typology of compound weather and climate events. *Nat. Rev. Earth Environ.* **1**, 333 (2020).
48. Hu, Z.-Z., L'Heureux, M., Kumar, A. & Becke, E. ENSO and the tropical Pacific, in state of the climate in 2022. *Bull. Am. Meteorol. Soc.* **104**, S213–S217 (2023).
49. Matthews, A. J. A multiscale framework for the origin and variability of the South Pacific Convergence Zone. *Q. J. R. Meteorol. Soc.* **138**, 1165–1178 (2012).
50. Kessler, W. S. EOF representation of the Madden–Julian Oscillation and its connection with ENSO. *J. Clim.* **14**, 3055–3061 (2001).
51. Clem, K. R., Renwick, J. A., McGregor, J. & Fogt, R. L. The relative influence of ENSO and SAM on Antarctic Peninsula climate. *J. Geophys. Res. Atmos.* **121**, 9324–9341 (2016).
52. Shields, C. A., Wille, J. D., Marquardt Collow, A. B., Maclennan, M. & Gorodetskaya, I. V. Evaluating uncertainty and modes of variability for Antarctic atmospheric rivers. *Geophys. Res. Lett.* **49**, e2022GL099577 (2022).
53. Marshall, G. J. Trends in the Southern Annular Mode from observations and reanalyses. *J. Clim.* **16**, 4134–4143 (2003).
54. Galperin, B., Sukoriansky, S. & Anderson, P. S. On the critical Richardson number in stably stratified turbulence. *Atmos. Sci. Lett.* **8**, 65–69 (2007).
55. Birner, T., Dörnbrack, A. & Schumann, U. How sharp is the tropopause at midlatitudes? *Geophys. Res. Lett.* **29**, 45-1–45-4 (2002).
56. Rodriguez Imazio, P., Dörnbrack, A., Urzua, R. D., Rivaben, N. & Godoy, A. Clear air turbulence observed across a tropopause fold over the Drake Passage—a case study. *J. Geophys. Res. Atmos.* **127**, e2021JD035908 (2022).
57. Vaughan, G., O'Connor, F. M. & Wareing, D. P. Observations of streamers in the troposphere and stratosphere using ozone Lidar. *J. Atmos. Chem.* **38**, 295–315 (2001).
58. Sprenger, M., Croci Maspoli, M. & Wernli, H. Tropopause folds and cross-tropopause exchange: a global investigation based upon ECMWF analyses for the time period March 2000 to February 2001. *J. Geophys. Res.* **108**, 8518 (2003).
59. Rondanelli, R. et al. Strongest MGO on record triggers extreme Atacama rainfall and warmth in Antarctica. *Geophys. Res. Lett.* **46**, 3482–3491 (2019).
60. Turner, J. et al. Record low Antarctic sea ice cover in February 2022. *Geophys. Res. Lett.* **49**, e2022GL098904 (2022).
61. Wang, J. et al. An unprecedented record low Antarctic Sea-ice Extent during Austral Summer 2022. *Adv. Atmos. Sci.* **39**, 1591–1597 (2022).
62. A crumbling ice shelf edge after a warm summer and low sea ice: National Snow and Ice Data Center (NSIDC) newsletter published on 27 March 2023. https://nsidc.org/ice-sheets-today/analyses/crumbling-ice-shelf-edge-after-warm-summer-and-low-sea-ice (2023).
63. Ochwat, N., Banwell, A. & Scambos, T. Sidebar 6.2: Larsen B fast-ice breakout and initial glacier response, in State of the Climate in 2022. *Bull. Am. Meteorol. Soc.* **104**, S349–S351 (2023).
64. Bromwich, D. H. et al. The Year of Polar Prediction in the Southern Hemisphere (YOPP-SH). *Bull. Am. Meteorol. Soc.* **101**, E1653–E1676 (2020).
65. Tewari, K., Mishra, S. K., Salunke, P. & Dewarn, A. Future projections of temperature and precipitation for Antarctica. *Environ. Res. Lett.* **17**, 014029 (2022).

66. Bozkurt, D. et al. Temperature and precipitation projections for the Antarctic Peninsula over the next two decades: contrasting global and regional climate model simulations. *Clim. Dyn.* **56**, 3853–3874 (2021).
67. Feron, S. et al. Warming events projected to become more frequent and last longer across Antarctica. *Sci. Rep.* **11**, 1–9 (2021).
68. Stott, P. A. et al. Attribution of extreme weather and climate-related events. *WIREs Clim. Change* **7**, 23–41 (2016).
69. Kittel, C. et al. Diverging future surface mass balance between the Antarctic ice shelves and grounded ice sheet. *Cryosphere* **15**, 1215–1236 (2021).
70. Alley, K. E., Scambos, T. A., Miller, J. Z., Long, D. G. & MacFerrin, M. Quantifying vulnerability of Antarctic ice shelves to hydrofracture using microwave scattering properties. *Remote Sens. Environ.* **210**, 297–306 (2018).
71. Hersbach, H. et al. The ERA5 global reanalysis. *Q J. R. Meteorol. Soc.* **146**, 1999–2049 (2020).
72. Muñoz-Sabater, J. et al. ERA5-Land: a state-of-the-art global reanalysis dataset for land applications. *Earth Syst. Sci. Data* **13**, 4349–4383 (2021).
73. Agosta, C. et al. Estimation of the Antarctic surface mass balance using the regional climate model MAR (1979–2015) and identification of dominant processes. *Cryosphere* **13**, 281–296 (2019).
74. Lambin, C., Fettweis, X., Kittel, C., Fonder, M. & Ernst, D. Assessment of future wind speed and wind power changes over South Greenland using the Modèle Atmosphérique Régional regional climate model. *Int. J. Climatol.* **43**, 558–574 (2023).
75. Howat, I. M., Porter, C., Smith, B. E., Noh, M.-J. & Morin, P. The Reference Elevation Model of Antarctica. *Cryosphere* **13**, 665–674 (2019).
76. Dethinne, T. et al. Sensitivity of the MAR regional climate model snowpack to the parameterization of the assimilation of satellite-derived wet-snow masks on the Antarctic Peninsula. *Cryosphere* **17**, 4267–4288 (2023).
77. Picard, G. Snow status (wet/dry) in Antarctica from AMSR-E and AMSR2 passive microwave radiometers 2002 – 2023 [Data set]. Published via PerSCiDO. https://doi.org/10.18709/perscido.2023.04.ds391 (2023).
78. Picard, G. & Fily, M. Surface melting observations in Antarctica by microwave radiometers: correcting 26-year time series from changes in acquisition hours. *Remote Sens. Environ.* **104**, 325–336 (2006).
79. Torinesi, O., Fily, M. & Genthon, C. Variability and trends of the summer melt period of Antarctic Ice Margins since 1980 from microwave sensors. *J. Clim.* **16**, 1047–1060 (2003).
80. Takaya, K. & Nakamura, H. A formulation of a phase-independent wave-activity flux for stationary and migratory quasigeostrophic eddies on a zonally varying basic flow. *J. Atmos. Sci.* **58**, 608–627 (2001).
81. Henderson, S. A., Maloney, E. D. & Barnes, E. A. The influence of the Madden–Julian Oscillation on Northern Hemisphere winter blocking. *J. Clim.* **29**, 4597–4616 (2016).
82. Sardeshmukh, P. D. & Hoskins, B. J. The generation of global rotational flow by steady idealized tropical divergence. *J. Atmos. Sci.* **45**, 1228–1251 (1988).
83. Liebmann, B. & Smith, C. A. Description of a complete (interpolated) outgoing longwave radiation dataset. *Bull. Am. Meteorol. Soc.* **77**, 1275–1277 (1996).
84. Pisso, I. et al. The Lagrangian particle dispersion model FLEXPART version 10.4. *Geosci. Model Dev.* **12**, 4955–4997 (2019).
85. Coles, S. *An Introduction to Statistical Modeling of Extreme Values* (Springer Series in Statistics, Springer London, 2001).
86. Patterson, T. & Kelso, N. V. Antarctic Ice Shelf Edges, 1:50 million [Shapefile]. North American Cartographic Information Society. https://earthworks.stanford.edu/catalog/stanford-ms761jq9077 (2012).

ACKNOWLEDGEMENTS

This paper is a contribution to the Year of Polar Prediction in the Southern Hemisphere (YOPP-SH) international initiative and to the SCAR scientific research program AntClimNow. We thank Alicia Bentley for publicly available GFS-based maps, ECMWF for the operational forecasts provided to assist the Year of Polar Prediction in the Southern Hemisphere, and Antarctic Mesoscale Prediction System (AMPS) based on Polar WRF model maintained by Jordan Powers and Kevin Manning (NCAR) and Ohio State University Antarctic group, all of which helped to forecast the event. ERA5 and ERA5-Land data are available via ECMWF Copernicus Climate Change Service (C3S, https://cds.climate.copernicus.eu). We thank all national weather services listed in the "Data availability" section for providing station data. We thank the Chilean Antarctic Institute (INACH) for logistic support. I.V.G. thanks the support by the strategic funding to CIIMAR (UIDB/04423/2020, UIDP/04423/2020), CESAM (UIDP/50017/2020, UIDB/50017/2020, LA/P/0094/2020), 2021.03140.CEECIND, projects ATLACE (CIRCNA/CAC/0273/2019) and MAPS (2022.09201.PTDC) through national funds provided by FCT – Fundação para a Ciência e a Tecnologia. C.D.-A. was supported by postdoctoral fellowship in FCT project ATLACE (CIRCNA/CAC/0273/2019). I.V.G. and C.D.-A. thank FCT Portuguese Polar Program (PROPOLAR) for logistic support for the Antarctic fieldwork projects conducted in February 2022. K.R.C. acknowledges funding from the Royal Society of New Zealand Marsden Fund grant MFP-VUW2010. S.-J.P. was supported by the Korea Polar Research Institute (KOPRI) grant funded by the Ministry of Oceans and Fisheries (KOPRI PE23030). J.D.W. and V.F. acknowledge support from the Agence Nationale de la Recherche project, ANR-20-CE01–0013 (ARCA). P.R. and X.Z. were supported by National Science Foundation grants 2127632 and 2229392. J.C. thanks ANID-FONDECYT Project No. 1221122. RRC thanks the support of INACH (RT_69–20), ANID (FONDECYT 1191932 & ANILLO ACT210046), and CORFO (19BP-117358). M.L. was supported by the National Science Foundation Grant 1951603. A.M.G acknowledges partial support from the Argentinian grants UBACyT (UBA), PIP-CONICET-11220130100439CO, and PNRA for providing the necessary materials for the soundings, IAA, and SMN for forecasts and logistic support. S.K. and A.C. were supported by the Ukrainian State Special-Purpose Research Program in Antarctica for 2011–2023. T.D. thanks Consortium des Equipements de Calcul Intensif (CECI) for the computer resources, the Fonds de la Recherche Scientifique de Belgique (F.R.S. – FNRS, grant #2.5020.11) and the Tier-1 supercomputer (Nic5) of the Fédération Wallonie Bruxelles infrastructure funded by the Walloon Region (grant #1117545). Special thanks to Christoph Kittel for the help on the MAR data processing and evaluation.

AUTHOR CONTRIBUTIONS

I.V.G. initiated the research, analyzed data, produced and edited plots, designed and wrote all sections of the original paper, with input from coauthors revising the text. C.D.-A. made substantial contribution to sections "AP temperature and surface melt records" and "Atmospheric river and local drivers" with data analysis and plotting. S.G.-H. made substantial contributions to sections "AP temperature and surface melt records" and "February 2022 event in the context of climate change" with long-term and analog analysis. K.R.C. made substantial contribution to section "Large-scale drivers, upper troposphere configuration and moisture sources" with plots, analysis and writing. X.Z. and P.R. made substantial contribution with plots and analysis for section "Atmospheric river and local drivers." X.Z. conducted Polar WRF simulations. P.R.I. contributed to section "Large-scale drivers, upper troposphere configuration and moisture sources" with plotting Fig. 6g–j, analysis and writing. J.D.W. contributed with plotting Fig. 8. C.L.-D.S. and N.D. contributed to section "Large-scale drivers, upper troposphere configuration and moisture sources" with Fig. 9 and back trajectory analysis. D.C. conducted radiosonde launches at Escudero during the AR event and data analysis. S.G.-H., D.C., R.R.C., S.-J.P., A.M.G., P.R.I., S.C., A.C., S.K., J.C., and F.M.R. contributed with ground-based and/or radiosonde observations and their interpretation. M.A.L. and X.Z. contributed with satellite data analysis. V.F. and B.P. helped with valuable discussions and substantial contributions throughout the paper text. J.B. substantially contributed to section "February 2022 event in the context of climate change" with return periods analysis. T.D. contributed with MAR model simulations. G.P. contributed with surface melt satellite observations and interpretation. All authors provided comments to the manuscript.

COMPETING INTERESTS

The authors declare no competing interests.

ADDITIONAL INFORMATION

Supplementary information The online version contains supplementary material available at https://doi.org/10.1038/s41612-023-00529-6.

Correspondence and requests for materials should be addressed to Irina V. Gorodetskaya.

Reprints and permission information is available at http://www.nature.com/reprints

Publisher's note Springer Nature remains neutral with regard to jurisdictional claims in published maps and institutional affiliations.